

2016

New measurement of $\theta(13)$ via neutron capture on hydrogen at Daya Bay

F. P. An

E China Univ Sci & Technol, Inst Modern Phys, Shanghai 200237, Peoples R China;

A. B. Balantekin

Univ Wisconsin, Madison, WI 53706 USA;

J. J. Cherwinka

Univ Wisconsin, Madison, WI 53706 USA;

R. D. McKeown

College of William & Mary, Williamsburg, VA 23187 USA

W. Wang

College of William & Mary, Williamsburg, VA 23187 USA

Follow this and additional works at: <https://scholarworks.wm.edu/aspubs>

Recommended Citation

An, F. P., Balantekin, A. B., Band, H. R., Bishai, M., Blyth, S., Cao, D., ... & Chang, J. F. (2016). New measurement of $\theta 13$ via neutron capture on hydrogen at Daya Bay. *Physical Review D*, 93(7), 072011.

This Article is brought to you for free and open access by the Arts and Sciences at W&M ScholarWorks. It has been accepted for inclusion in Arts & Sciences Articles by an authorized administrator of W&M ScholarWorks. For more information, please contact scholarworks@wm.edu.

New measurement of θ_{13} via neutron capture on hydrogen at Daya Bay

F. P. An,¹ A. B. Balantekin,² H. R. Band,³ M. Bishai,⁴ S. Blyth,^{5,6} D. Cao,⁷ G. F. Cao,⁸ J. Cao,⁸ W. R. Cen,⁸ Y. L. Chan,⁹ J. F. Chang,⁸ L. C. Chang,¹⁰ Y. Chang,⁶ H. S. Chen,⁸ Q. Y. Chen,¹¹ S. M. Chen,¹² Y. X. Chen,¹³ Y. Chen,¹⁴ J. H. Cheng,¹⁰ J.-H. Cheng,¹⁰ J. Cheng,¹¹ Y. P. Cheng,⁸ Z. K. Cheng,¹⁵ J. J. Cherwinka,² M. C. Chu,⁹ A. Chukanov,¹⁶ J. P. Cummings,¹⁷ J. de Arcos,¹⁸ Z. Y. Deng,⁸ X. F. Ding,⁸ Y. Y. Ding,⁸ M. V. Diwan,⁴ M. Dolgareva,¹⁶ J. Dove,¹⁹ D. A. Dwyer,²⁰ W. R. Edwards,²⁰ R. Gill,⁴ M. Gonchar,¹⁶ G. H. Gong,¹² H. Gong,¹² M. Grassi,⁸ W. Q. Gu,²¹ M. Y. Guan,⁸ L. Guo,¹² R. P. Guo,⁸ X. H. Guo,²² Z. Guo,¹² R. W. Hackenburg,⁴ R. Han,¹³ S. Hans,⁴ M. He,⁸ K. M. Heeger,³ Y. K. Heng,⁸ A. Higuera,²³ Y. K. Hor,²⁴ Y. B. Hsiung,⁵ B. Z. Hu,⁵ T. Hu,⁸ W. Hu,⁸ E. C. Huang,¹⁹ H. X. Huang,²⁵ X. T. Huang,¹¹ P. Huber,²⁴ W. Huo,²⁶ G. Hussain,¹² D. E. Jaffe,⁴ P. Jaffke,²⁴ K. L. Jen,¹⁰ S. Jetter,⁸ X. P. Ji,^{27,12} X. L. Ji,⁸ J. B. Jiao,¹¹ R. A. Johnson,²⁸ J. Joshi,⁴ L. Kang,²⁹ S. H. Kettell,⁴ S. Kohn,³⁰ M. Kramer,^{20,30} K. K. Kwan,⁹ M. W. Kwok,⁹ T. Kwok,³¹ T. J. Langford,³ K. Lau,²³ L. Lebanowski,¹² J. Lee,²⁰ J. H. C. Lee,³¹ R. T. Lei,²⁹ R. Leitner,³² J. K. C. Leung,³¹ C. Li,¹¹ D. J. Li,²⁶ F. Li,⁸ G. S. Li,²¹ Q. J. Li,⁸ S. Li,²⁹ S. C. Li,^{31,24} W. D. Li,⁸ X. N. Li,⁸ Y. F. Li,⁸ Z. B. Li,¹⁵ H. Liang,²⁶ C. J. Lin,²⁰ G. L. Lin,¹⁰ S. Lin,²⁹ S. K. Lin,²³ Y.-C. Lin,⁵ J. J. Ling,¹⁵ J. M. Link,²⁴ L. Littenberg,⁴ B. R. Littlejohn,¹⁸ D. W. Liu,²³ J. J. Liu,³¹ J. L. Liu,²¹ J. C. Liu,⁸ C. W. Loh,⁷ C. Lu,³³ H. Q. Lu,⁸ J. S. Lu,⁸ K. B. Luk,^{30,20} Z. Lv,³⁴ Q. M. Ma,⁸ X. Y. Ma,⁸ X. B. Ma,¹³ Y. Q. Ma,⁸ Y. Malyskin,³⁵ D. A. Martinez Caicedo,¹⁸ K. T. McDonald,³³ R. D. McKeown,^{36,37} I. Mitchell,²³ M. Mooney,⁴ Y. Nakajima,²⁰ J. Napolitano,³⁸ D. Naumov,¹⁶ E. Naumova,¹⁶ H. Y. Ngai,³¹ Z. Ning,⁸ J. P. Ochoa-Ricoux,³⁵ A. Olshevskiy,¹⁶ H.-R. Pan,⁵ J. Park,²⁴ S. Patton,²⁰ V. Pec,³² J. C. Peng,¹⁹ L. Pinsky,²³ C. S. J. Pun,³¹ F. Z. Qi,⁸ M. Qi,⁷ X. Qian,⁴ N. Raper,³⁹ J. Ren,²⁵ R. Rosero,⁴ B. Roskovec,³² X. C. Ruan,²⁵ H. Steiner,^{30,20} G. X. Sun,⁸ J. L. Sun,⁴⁰ W. Tang,⁴ D. Taychenachev,¹⁶ T. Konstantin,¹⁶ K. V. Tsang,²⁰ C. E. Tull,²⁰ N. Viaux,³⁵ B. Viren,⁴ V. Vorobel,³² C. H. Wang,⁶ M. Wang,¹¹ N. Y. Wang,²² R. G. Wang,⁸ W. Wang,^{37,15} W. W. Wang,⁷ X. Wang,⁴¹ Y. F. Wang,⁸ Z. Wang,¹² Z. Wang,⁸ Z. M. Wang,⁸ H. Y. Wei,¹² L. J. Wen,⁸ K. Whisnant,⁴² C. G. White,¹⁸ L. Whitehead,²³ T. Wise,² H. L. H. Wong,^{30,20} S. C. F. Wong,¹⁵ E. Worcester,⁴ C.-H. Wu,¹⁰ Q. Wu,¹¹ D. M. Xia,^{43,8} J. K. Xia,⁸ Z. Z. Xing,⁸ J. Y. Xu,⁹ J. L. Xu,⁸ J. Xu,²² Y. Xu,¹⁵ T. Xue,¹² J. Yan,³⁴ C. G. Yang,⁸ H. Yang,⁷ L. Yang,²⁹ M. S. Yang,⁸ M. T. Yang,¹¹ M. Ye,⁸ Z. Ye,²³ M. Yeh,⁴ B. L. Young,⁴² G. Y. Yu,⁷ Z. Y. Yu,⁸ L. Zhan,⁸ C. Zhang,⁴ H. H. Zhang,¹⁵ J. W. Zhang,⁸ Q. M. Zhang,³⁴ X. T. Zhang,⁸ Y. M. Zhang,¹² Y. X. Zhang,⁴⁰ Y. M. Zhang,¹⁵ Z. J. Zhang,²⁹ Z. Y. Zhang,⁸ Z. P. Zhang,²⁶ J. Zhao,⁸ Q. W. Zhao,⁸ Y. F. Zhao,¹³ Y. B. Zhao,⁸ W. L. Zhong,⁸ L. Zhou,⁸ N. Zhou,²⁶ H. L. Zhuang,⁸ and J. H. Zou⁸

(The Daya Bay Collaboration)

¹*Institute of Modern Physics, East China University of Science and Technology, Shanghai*

²*University of Wisconsin, Madison, Wisconsin, USA*

³*Department of Physics, Yale University, New Haven, Connecticut, USA*

⁴*Brookhaven National Laboratory, Upton, New York, USA*

⁵*Department of Physics, National Taiwan University, Taipei*

⁶*National United University, Miao-Li*

⁷*Nanjing University, Nanjing*

⁸*Institute of High Energy Physics, Beijing*

⁹*Chinese University of Hong Kong, Hong Kong*

¹⁰*Institute of Physics, National Chiao-Tung University, Hsinchu*

¹¹*Shandong University, Jinan*

¹²*Department of Engineering Physics, Tsinghua University, Beijing*

¹³*North China Electric Power University, Beijing*

¹⁴*Shenzhen University, Shenzhen*

¹⁵*Sun Yat-Sen (Zhongshan) University, Guangzhou*

¹⁶*Joint Institute for Nuclear Research, Dubna, Moscow Region*

¹⁷*Siena College, Loudonville, New York, USA*

¹⁸*Department of Physics, Illinois Institute of Technology, Chicago, Illinois, USA*

¹⁹*Department of Physics, University of Illinois at Urbana-Champaign, Urbana, Illinois, USA*

²⁰*Lawrence Berkeley National Laboratory, Berkeley, California, USA*

²¹*Department of Physics and Astronomy, Shanghai Jiao Tong University,*

Shanghai Laboratory for Particle Physics and Cosmology, Shanghai

²²*Beijing Normal University, Beijing*

²³*Department of Physics, University of Houston, Houston, Texas, USA*

²⁴*Center for Neutrino Physics, Virginia Tech, Blacksburg, Virginia, USA*

²⁵*China Institute of Atomic Energy, Beijing*

²⁶University of Science and Technology of China, Hefei

²⁷School of Physics, Nankai University, Tianjin

²⁸Department of Physics, University of Cincinnati, Cincinnati, Ohio, USA

²⁹Dongguan University of Technology, Dongguan

³⁰Department of Physics, University of California, Berkeley, California, USA

³¹Department of Physics, The University of Hong Kong, Pokfulam, Hong Kong

³²Charles University, Faculty of Mathematics and Physics, Prague, Czech Republic

³³Joseph Henry Laboratories, Princeton University, Princeton, New Jersey, USA

³⁴Xi'an Jiaotong University, Xi'an

³⁵Instituto de Física, Pontificia Universidad Católica de Chile, Santiago, Chile

³⁶California Institute of Technology, Pasadena, California, USA

³⁷College of William and Mary, Williamsburg, Virginia, USA

³⁸Department of Physics, College of Science and Technology, Temple University, Philadelphia, Pennsylvania, USA

³⁹Department of Physics, Applied Physics, and Astronomy, Rensselaer Polytechnic Institute, Troy, New York, USA

⁴⁰China General Nuclear Power Group

⁴¹College of Electronic Science and Engineering, National University of Defense Technology, Changsha

⁴²Iowa State University, Ames, Iowa, USA

⁴³Chongqing University, Chongqing

This article reports an improved independent measurement of neutrino mixing angle θ_{13} at the Daya Bay Reactor Neutrino Experiment. Electron antineutrinos were identified by inverse β -decays with the emitted neutron captured by hydrogen, yielding a data-set with principally distinct uncertainties from that with neutrons captured by gadolinium. With the final two of eight antineutrino detectors installed, this study used 621 days of data including the previously reported 217-day data set with six detectors. The dominant statistical uncertainty was reduced by 49%. Intensive studies of the cosmogenic muon-induced ${}^9\text{Li}$ and fast neutron backgrounds and the neutron-capture energy selection efficiency, resulted in a reduction of the systematic uncertainty by 26%. The deficit in the detected number of antineutrinos at the far detectors relative to the expected number based on the near detectors yielded $\sin^2 2\theta_{13} = 0.071 \pm 0.011$ in the three-neutrino-oscillation framework. The combination of this result with the gadolinium-capture result is also reported.

PACS numbers: 14.60.Pq, 29.40.Mc, 28.50.Hw, 13.15.+g

Keywords: neutrino oscillation, hydrogen neutron-capture, reactor antineutrinos, Daya Bay

I. INTRODUCTION

Precise measurements of neutrino mixing parameters are crucial to searches for CP -symmetry violation among neutral leptons and tests of neutrino oscillation theory. In particular, the precision of neutrino mixing angle θ_{13} is of key significance in constraining the leptonic CP phase δ [1–4]. Prior to 2012, many experimental efforts had been made to determine θ_{13} [5–10]. The first measurement of θ_{13} with a significance greater than five standard deviations was reported by the Daya Bay Reactor Neutrino Experiment in 2012 [11]. The most recent determinations of θ_{13} from reactor and accelerator experiments [12–18] are consistent.

The three reactor antineutrino experiments, Double Chooz [19], RENO [20], and Daya Bay [21], currently provide the most precise measurements of the mixing angle. They use gadolinium-doped liquid scintillator to identify electron antineutrinos through inverse β -decay (IBD) reactions ($\bar{\nu}_e + p \rightarrow n + e^+$) with the neutron capturing on gadolinium ($n\text{Gd}$). A surrounding volume of undoped liquid scintillator improves the efficiency of detecting γ 's that escape from the doped volume, and has been used (in conjunction with the doped volume) by each of the three reactor experiments to determine $\sin^2 2\theta_{13}$ independently through IBD reactions with the neutron captured by hydrogen ($n\text{H}$) [14, 15, 22, 23]. The

KamLAND experiment has used $n\text{H}$ IBDs to measure the disappearance of reactor $\bar{\nu}_e$ [24] and the flux of geo- $\bar{\nu}_e$ [25]. The Super-Kamiokande experiment has used $n\text{H}$ IBDs to search for relic supernova $\bar{\nu}_e$ [26]. Future projects, including the medium-baseline reactor experiments JUNO [27] and RENO-50 [28], and LENA [29], will also make use of $n\text{H}$ IBDs. Techniques developed for this analysis may be useful for these future experiments.

The previous analysis of $n\text{H}$ IBDs from Daya Bay [15] is improved in this article with 3.6 times the number of detected IBDs and with reduced uncertainties of backgrounds and the neutron-capture energy selection efficiency. This statistically-independent measurement is also largely systematically independent from the $n\text{Gd}$ -IBD analysis, and improves the overall uncertainty of $\sin^2 2\theta_{13}$ from Daya Bay.

This article is organized as follows. Section II describes the Daya Bay experiment. The calculation of reactor antineutrino flux is described in Section III. Analysis of the data, including event reconstruction and IBD selection, is described in Section IV. Section V describes the accidental background, and Section VI describes correlated backgrounds. The IBD selection efficiency is discussed in Section VII. The fit for $\sin^2 2\theta_{13}$ and its combination with the $n\text{Gd}$ -IBD result are presented in Section VIII. Section IX briefly discusses the impact of the results and improvements expected in the future.

II. EXPERIMENT

Located in Guangdong province, China, the Daya Bay experiment measures electron antineutrinos emitted from three pairs of nuclear reactors, each reactor nominally producing 2.9 GW of thermal power. Inside the adjacent mountains, two *near* experimental halls (EH1 and EH2) are located roughly 360-470 m from their nearest reactor, and one *far* experimental hall (EH3) is located 1.52-1.93 km from all six reactors.

Each far (near) experimental hall contains 4 (2) antineutrino detectors (ADs) submerged in a two-zone water Cherenkov detector [30]. An inner and outer zone together provide each AD with > 2.5 m of shielding against ambient radiation and spallation products of nearby cosmogenic muons. These inner and outer water shields (IWS and OWS) are independent cosmogenic muon detectors with 160 (121) and 224 (167) 20-cm photomultiplier tubes (PMTs), respectively, in the far (near) hall(s). Detecting muons enables estimates of muon-induced backgrounds; particularly, $^9\text{Li}/^8\text{He}$ decay products and spallation neutrons.

The ADs were identically designed and consist of three nested, coaxial cylindrical vessels: an inner and outer acrylic vessel (IAV and OAV) [31] and an outermost stainless steel vessel (SSV), as shown in Fig. 1. For future reference, the z coordinate is defined by the central axis of the cylinders and the r coordinate is measured radially from the central axis. The IAV is about 3 m in both height and diameter, and holds 20 tons of gadolinium-

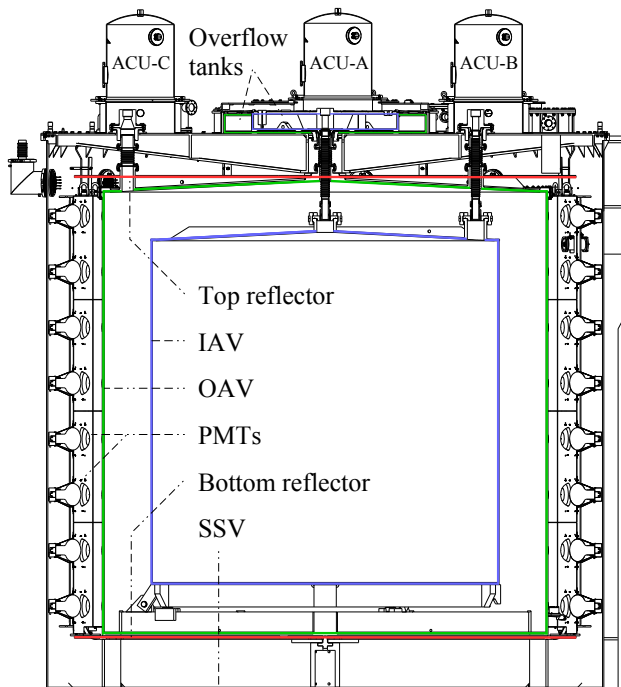


FIG. 1. Schematic of an antineutrino detector. See the text for definitions.

doped (0.1% by mass) liquid scintillator (GdLS) [32]. The surrounding OAV is about 4 m in both height and diameter, and holds 22 tons of undoped liquid scintillator (LS) to improve the efficiency of detecting γ 's that escape from the GdLS. The surrounding SSV is about 5 m in both height and diameter, and holds 36 tons of mineral oil (MO) to shield against radiation from the PMTs and the SSV.

Each AD contains 192 20-cm PMTs arranged in 24 columns and 8 rings at a fixed radius ($r \approx 2.19$ m) in the MO. Reflectors were installed above and below the OAV to improve light collection. Three automated calibration units (ACUs) are affixed atop each AD and house LEDs and various radioactive sources for calibrating the energy scale and position reconstruction of events in the ADs [33]. The ACUs deploy vertically at three radial positions: ACU-A at the center ($r = 0$), ACU-B near the wall of the IAV ($r = 1.35$ m), and ACU-C near the wall of the OAV ($r = 1.77$ m).

ADs were triggered, and recorded the time and charge information of each PMT channel, when the number of PMTs with pulses above threshold (N_{PMT}) was ≥ 45 or when the integrated sum of PMT pulses from all 192 PMTs (Q_{sum}) was $\gtrsim 65$ photoelectrons. Both trigger thresholds corresponded to approximately 0.4 MeV and accepted 100% of IBD positrons with > 0.7 MeV of deposited energy [34]. Water shields triggered independently under analogous conditions [30]. The trigger criteria were tested within each cycle of an 80-MHz clock, and if satisfied, the subsequent $1 \mu\text{s}$ (and preceding 200 ns) of data from all channels were recorded. The physical interactions that caused a single trigger in a given detector are referred to as an “event”. The time of an event is defined as the time of the trigger.

More detailed descriptions of the detector hardware are given in Ref. [35].

The analysis presented in this article determines $\sin^2 2\theta_{13}$ by counting interactions of reactor antineutrinos in each AD in the one far and two near experimental halls. Antineutrinos were identified in both the GdLS and LS volumes via IBD reactions ($\bar{\nu}_e + p \rightarrow n + e^+$) in which the positron carried away 99.4% of the kinetic energy of the final state on average. The positron deposited energy within $O(1)$ ns and then annihilated with an electron, usually producing two back-to-back 0.511-MeV γ 's (several percent of the positrons annihilated in flight such that the sum of γ energies was greater than 2×0.511 MeV). The neutron thermalized and was captured primarily by Gd or H, releasing an approximately 8-MeV γ cascade or a single 2.22-MeV γ , respectively. The time from production to capture was typically tens to hundreds of microseconds. The temporal coincidence of the prompt positron and delayed neutron-capture clearly distinguishes antineutrinos from single-event backgrounds.

III. REACTOR ANTINEUTRINO FLUX

The expected number of IBDs in an AD was calculated as the product of the number of IBDs per target proton Φ and the efficiency-weighted number of target protons N_ε :

$$\overline{N}_{\text{IBD}} = \Phi N_\varepsilon. \quad (1)$$

The latter is discussed in Section VII and the former is defined for the d -th AD as

$$\Phi_d \equiv \sum_{r=1}^6 \frac{1}{4\pi L_{dr}^2} \iint_{\{t_d\}} \sigma_\nu(E) P_\nu\left(\frac{L_{dr}}{E}\right) \frac{d^2 N_r(E, t)}{dE dt} dE dt, \quad (2)$$

where L_{dr} is the baseline distance between the d -th AD and the r -th reactor core, $\sigma_\nu(E)$ is the IBD reaction cross-section of an antineutrino with energy E , $P_\nu(L_{dr}/E)$ is the neutrino survival probability, and $d^2 N_r(E, t)/dE dt$ is the number of antineutrinos emitted from the r -th reactor at time t with energy E , which is integrated over the periods of data acquisition for the d -th AD $\{t_d\}$.

The baselines L_{dr} [36] were measured with negligible uncertainty [35]. The cross-section σ_ν was evaluated according to Ref. [37] using physical parameters from Ref. [38]. In the three-neutrino-oscillation framework, the survival probability of electron (anti)neutrinos is expressed as

$$P_\nu = 1 - \cos^4 \theta_{13} \sin^2 2\theta_{12} \sin^2 \Delta_{21} - \sin^2 2\theta_{13} \cos^2 \theta_{12} \sin^2 \Delta_{31} - \sin^2 2\theta_{13} \sin^2 \theta_{12} \sin^2 \Delta_{32}, \quad (3)$$

where $\Delta_{ij} \equiv 1.267 \Delta m_{ij}^2 L/E$, E [MeV] is the energy of the neutrino at production, L [m] is the distance between the points of production and interaction of the neutrino, and Δm_{ij}^2 [eV²] is the difference between the squared masses of mass eigenstates ν_i and ν_j . The values of $\sin^2 2\theta_{12} = 0.846 \pm 0.021$, $\Delta m_{21}^2 = (7.53 \pm 0.18) \times 10^{-5}$ eV², and $\Delta m_{32}^2 = (2.44 \pm 0.06) \times 10^{-3}$ eV² (for the normal hierarchy) [$\Delta m_{32}^2 = (2.52 \pm 0.07) \times 10^{-3}$ eV² (for the inverted hierarchy)] were taken from Ref. [38]. These uncertainties were found to have negligible impact on the fit of $\sin^2 2\theta_{13}$ and its uncertainty. The reactor antineutrino emission rate was calculated as

$$\frac{d^2 N(E, t)}{dE dt} = \frac{W_{\text{th}}(t)}{\sum_i f_i(t) e_i} \sum_i f_i(t) S_i(E) c_i^{\text{ne}}(E, t) + S_{\text{snf}}(E, t), \quad (4)$$

where the sum is over the four primary fissile isotopes: ²³⁵U, ²³⁹Pu, ²³⁸U, ²⁴¹Pu. The thermal power of the reactor $W_{\text{th}}(t)$ and fraction of fissions due to the i -th isotope $f_i(t)$ were supplied by the nuclear power plant, the average thermal energies released per fission e_i were from Ref. [39], the antineutrino yields per fission $S_i(E)$ from ²³⁸U, and from ²³⁵U, ²³⁹Pu, and ²⁴¹Pu, were from Ref. [40] and Ref. [41], respectively. The correction to

the energy spectrum due to non-equilibrium effects of long-lived fission fragments $c_i^{\text{ne}}(E, t)$ followed Ref. [40]. The contribution from spent nuclear fuel $S_{\text{snf}}(E, t)$ was estimated following Refs. [42, 43]. Combining the uncertainties of these components gave a 0.9% reactor-uncorrelated uncertainty of predicted IBD rate associated with a single reactor [44]. Additional information is given in Refs. [44, 45]. These quantities were estimated on a daily basis, weighted by the fractional data acquisition time of each day for each experimental hall, and then summed for each week. The accumulated predicted spectra $dN_r(E)/dE$ are provided [36].

IV. DATA ANALYSIS

The data used in this analysis were recorded beginning on December 24, 2011, with two ADs in EH1, one in EH2, and three in EH3. Recording was paused on July 28, 2012, to install the final two ADs in EH2 and EH3. On October 19, 2012, recording resumed with the full-design configuration of eight ADs. The first measurement with n H IBDs at Daya Bay [15] used the 217 days of data recorded in the six-AD configuration while this study uses an additional 404 days of data recorded in the full eight-AD configuration until November 27, 2013. Data acquisition maintained an operational efficiency of $> 97\%$ with occasional pauses for maintenance. Excluding weekly calibrations, special calibrations, and problematic data, the data acquisition (DAQ) time T_{DAQ} of each AD is listed in Table II. With the n H selection criteria described in the following sections, about 780000 IBDs were observed.

IV.1. Calibration and reconstruction

The gain [analog-to-digital converter channel/photoelectron] of each PMT channel was calibrated *in situ* by fitting the single photoelectron peak in the PMT dark noise spectrum. The peak was fit with a Poisson-Gaussian convolution [35]. This gain calibration was validated by an independent method using low-intensity LED pulses. The energy scale [MeV/photoelectron] of each AD was calibrated *in situ* with muon-induced spallation neutrons that captured on Gd throughout the GdLS volume. The two isotopes ¹⁵⁷Gd and ¹⁵⁵Gd, which release γ -cascades of 7.94 and 8.54 MeV, respectively, were fit with two Crystal Ball functions [46] as described in Ref. [34]. This energy scale calibration was validated by an independent method using weekly deployments of the ⁶⁰Co γ source of ACU A at the center of each AD.

The energy scale of an AD increased by 10-15% from the center of the detector to the wall of the OAV, and changed by 2-6% between the bottom and the top of the OAV, depending on the radial position. Corrections of energy scale as a function of position were applied with

two-dimensional maps (z vs. r) derived from spallation neutron-captures on Gd in each AD. The maps were extrapolated to the LS volume using spallation neutron-captures on H throughout the GdLS and LS volumes. The energy after correction is referred to as the “reconstructed” energy E_{rec} . Using $n\text{H}$ γ ’s, the standard deviation of E_{rec} across an AD was observed to be less than 1.0% for all ADs. The energy resolution was measured to be roughly $9\%/\sqrt{E_{\text{rec}}[\text{MeV}]}$ at the center of an AD. It improved by around 20% (relative) from the center to the wall of the OAV.

A single position associated with each event in an AD was “reconstructed” using charge-pattern templates derived from Monte Carlo simulation [34]. From a simulation of positrons, the average distribution of charge from the 192 PMT channels, or the charge-pattern, was determined for each of 9600 voxels within the OAV, corresponding to 20, 20, and 24 divisions in r^2 , z , and ϕ (where symmetry of ϕ was assumed to decrease statistical uncertainty). For each event, a χ^2 was calculated for each voxel using the expected (from the templates) and observed charges from each PMT channel. The voxel with the smallest χ^2 was selected and, with its nearest-neighbor voxels, interpolated to obtain the reconstructed position. The reconstructed positions of prompt events (see Section IV.2) are shown in Figs. 2(e) and 2(f), where a residual voxel grid is apparent. The resolution for a 2.2-MeV γ was about 12 cm in the r - ϕ plane and 13 cm along the z axis, in the LS volume. The position resolution improved by more than 40% from the center of a detector to the wall of an OAV, and varied within a few percent vertically. Using the ^{60}Co γ sources of the ACUs, the bias of the reconstruction was found to be about four times smaller than the resolution, near the wall of an OAV.

IV.2. IBD Candidate Selection

IBD candidates were selected from pairs of successive events in an AD, excluding those within predefined time ranges of detected muons to suppress muon-induced backgrounds. The IBD selection criteria for the $n\text{Gd}$ -[12] and $n\text{H}$ -IBD analyses are listed in Table I. First, AD events caused by spontaneous light emission from PMTs (PMT flashes) were removed as described in Section IV.2.1. Then, for the $n\text{H}$ -IBD analysis, AD events were required to have $E_{\text{rec}} > 1.5$ MeV to exclude low-energy backgrounds (see Section IV.2.2). The AD events remaining after muon-event vetoes (see Section IV.2.3) were grouped within a time window to identify double coincidences (see Section IV.2.4). The resulting prompt and delayed events were required to have $E_{\text{rec}} < 12$ MeV and E_{rec} within three standard deviations of the fitted $n\text{H}$ γ energy in each AD, respectively. Finally, the distance between the reconstructed positions of the prompt and delayed events was required to be within 50 cm to suppress uncorrelated double coincidences (accidentals), which dominated the set of double coincidences (see Sec-

	$n\text{H}$	$n\text{Gd}$
AD trigger	$N_{\text{PMT}} \geq 45$ OR $Q_{\text{sum}} \gtrsim 65$ p.e.	
20-cm PMT flash	$Ellipse < 1$	
5-cm PMT flash	$Q < 100$ p.e.	
Low energy	> 1.5 MeV	> 0.7 MeV
Detector latency	< 2 μs	
WS muon (μ_{WS}) [IWS/OWS]	$N_{\text{PMT}} > 12/15$	$N_{\text{PMT}} > 12/12$
AD muon (μ_{AD})	> 20 MeV	
Showering AD muon (μ_{sh})	> 2.5 GeV	
WS muon veto	(0, 400) μs	(-2, 600) μs
AD muon veto	(0, 800) μs	(-2, 1000) μs
Showering AD muon veto	(0 μs , 1 s)	(-2 μs , 1 s)
Coincidence time (t_c)	[1, 400] μs	[1, 200] μs
Prompt energy (E_p)	< 12 MeV	
Delayed energy (E_d)	peak $\pm 3\sigma$	[6, 12] MeV
Coincidence distance (d_c)	< 50 cm	NA

TABLE I. IBD selection criteria for the $n\text{H}$ and $n\text{Gd}$ [12] analyses. See text for details.

tion IV.2.5). The resulting number of $n\text{H}$ -IBD candidates (N_{DC}) is listed in Table II for each AD. Details of the selection criteria are described below.

IV.2.1. PMT Flashes

PMT flashes are spontaneous emissions of light from the voltage divider of a PMT. AD events caused by a flash from any one of the 192 20-cm PMTs were removed by requiring $Ellipse \equiv \sqrt{Quadrant^2 + (q_{\text{max}}/0.45)^2} < 1$, where q_{max} is the largest fraction of an AD event’s total charge in a single PMT and $Quadrant$ is defined as $Q_3/(Q_2 + Q_4)$ in which Q_i is the total charge in AD azimuthal quadrant i and quadrant 1 is approximately centered on the PMT with q_{max} . The efficiency of this criterion to select IBDs in the combined GdLS plus LS volume was estimated with Monte Carlo simulation [45] to be $> 99.99\%$. Flashes from six 5-cm calibration PMTs [35] near the top and bottom reflectors were simply removed by requiring the charge output from each 5-cm PMT to be < 100 photoelectrons.

IV.2.2. Low-energy Criterion

AD events were required to have $E_{\text{rec}} > 1.5$ MeV to exclude events caused by correlated β - α decays from the ^{214}Bi - ^{214}Po - ^{210}Pb and ^{212}Bi - ^{212}Po - ^{208}Pb decay chains, which originate from naturally-occurring ^{238}U and ^{232}Th , respectively. Due to the greater quenching associated with α ’s, the 8.78-MeV α from the latter chain resulted in an apparent energy of $E_{\text{rec}} = 1.26$ MeV and the 7.68-MeV α from the former chain resulted in $E_{\text{rec}} = 1.00$ MeV. Excluding these decays reduced the uncertainty of the total rate of accidentals by an order of magnitude. This criterion rejected about 10% of IBD prompt events.

	EH1-AD1	EH1-AD2	EH2-AD1	EH2-AD2	EH3-AD1	EH3-AD2	EH3-AD3	EH3-AD4
T_{DAQ} [d]	565.436	565.436	568.019	378.407	562.414	562.414	562.414	372.685
ε_{μ}	0.7949	0.7920	0.8334	0.8333	0.9814	0.9814	0.9812	0.9814
ε_m	0.9844	0.9845	0.9846	0.9846	0.9844	0.9841	0.9839	0.9845
R_{μ} [Hz]	200.32	200.32	150.08	149.80	15.748	15.748	15.748	15.757
R_s [Hz]	20.111	19.979	19.699	19.702	19.651	20.020	20.182	19.649
N_{DC}	217613	219721	208606	136718	56880	56106	59230	38037
N_{Acc}	26240 \pm 49	25721 \pm 49	25422 \pm 43	16365 \pm 29	29920 \pm 19	30065 \pm 20	32179 \pm 21	20427 \pm 15
N_{Cor}	191373 \pm 473	194000 \pm 475	183184 \pm 465	120353 \pm 449	26960 \pm 246	26041 \pm 244	27051 \pm 251	17610 \pm 196
R_{Acc} [d^{-1}]	59.31 \pm 0.11	58.34 \pm 0.11	54.54 \pm 0.09	52.71 \pm 0.09	55.07 \pm 0.04	55.35 \pm 0.04	59.27 \pm 0.04	56.73 \pm 0.04
R_{Li9} [d^{-1}]	2.36 \pm 1.02		1.73 \pm 0.75		0.19 \pm 0.09			
R_{FastN} [d^{-1}]	2.11 \pm 0.18		1.81 \pm 0.17		0.16 \pm 0.03			
R_{AmC} [d^{-1}]	0.07 \pm 0.04	0.07 \pm 0.04	0.07 \pm 0.03	0.07 \pm 0.03	0.03 \pm 0.02	0.03 \pm 0.02	0.03 \pm 0.02	0.02 \pm 0.01
R_{IBD} [d^{-1}]	428.01 \pm 1.48	435.49 \pm 1.49	389.41 \pm 1.25	384.03 \pm 1.42	49.24 \pm 0.45	47.56 \pm 0.45	49.44 \pm 0.46	48.54 \pm 0.55
$n\text{H}/n\text{Gd}$	0.993 \pm 0.007	0.993 \pm 0.007	0.995 \pm 0.007	0.995 \pm 0.008	1.015 \pm 0.012	0.981 \pm 0.012	1.019 \pm 0.012	0.987 \pm 0.014

TABLE II. Data summary for each AD. All per-day rates are corrected with $\varepsilon_{\mu}\varepsilon_m$. T_{DAQ} is the DAQ time, ε_{μ} is the muon-veto efficiency, ε_m is the multiplicity selection efficiency, R_{μ} is the muon rate, R_s is the rate of uncorrelated single events, N_{DC} is the number of double-coincidence (DC) events satisfying all IBD selection criteria, N_{Acc} is the number of accidental DCs, N_{Cor} is the number of correlated DCs, R_{Acc} , R_{Li9} , R_{FastN} , R_{AmC} , and R_{IBD} are the rates of accidental, fast neutron, ${}^9\text{Li}/{}^8\text{He}$, Am-C, and IBD (with all the backgrounds subtracted) DCs, and $n\text{H}/n\text{Gd}$ is the ratio of the efficiency- and target proton-corrected R_{IBD} for the $n\text{H}$ - and $n\text{Gd}$ -IBD analyses. The differences in R_{IBD} among ADs in the same near hall are due primarily to differences in baselines to the reactors, and secondarily to differences in target mass.

IV.2.3. Muon-event Vetoes

To suppress backgrounds from muon-induced spallation neutrons (Section VI.2) and long-lived spallation products such as ${}^9\text{Li}$ and ${}^8\text{He}$ (Section VI.1), an AD event was excluded from the analysis if it occurred within pre-defined veto time windows after cosmogenic muon events identified by the water shields or ADs. Muon events from the ADs, IWS, and OWS that occurred within the 2- μs detector latency were grouped together for the accounting of all events associated with cosmogenic muons. The muon event with the earliest time in the group defined the start of the muon-veto time window.

A muon event in a water shield, referred to as a μ_{WS} , was defined by requiring $N_{\text{PMT}} > 12$ (15) in the IWS (OWS). The muon-detection efficiency of these selections was essentially 100%, as determined relative to the ADs [30]. The higher threshold of the OWS in the $n\text{H}$ -IBD analysis (see Table I) removed correlated triggers that sometimes occurred $O(100)$ μs after an OWS event, due to electronics noise. These triggers were handled in the $n\text{Gd}$ -IBD analysis by slightly modifying the multiple-coincidence criteria (see Section IV.2.4) to have no overlap with a muon-veto time window.

An AD event that was grouped with a μ_{WS} and with 20 $\text{MeV} < E_{\text{rec}} < 2.5$ GeV was defined as an AD muon event μ_{AD} . If instead, $E_{\text{rec}} > 2.5$ GeV , the event was defined as a showering AD muon event μ_{sh} . The total rate of muon events measured by each AD (R_{μ}) is listed in Table II.

An AD event was excluded if it occurred within a veto time window of 400 μs , 800 μs , or 1 s after a μ_{WS} , μ_{AD} , or μ_{sh} , respectively. The fraction of DAQ time remaining for IBD analysis after implementing these offline muon-

veto is reported as ε_{μ} in Table II, with typical values of 79%, 83% and 98% in EH1, EH2, and EH3, respectively.

IV.2.4. Coincidence Time

Correlated AD events were selected using a coincidence time window of [1, 400] μs , which is about two times longer than the mean capture time of an IBD neutron on hydrogen in LS and about 14 times longer than that in GdLS. Given the data recording window of 1 μs , coincidence windows were initiated 1 μs after an event to ensure distinction of prompt and delayed events. Lone events are denoted as “singles” and were used to construct accidental background samples (see Section V). Only pairs of events, denoted as double coincidences (DCs), were used to select IBD candidates. If more than two events occurred within [1, 400] μs , they were excluded from further analysis. In addition, if the first, or prompt, event of a DC occurred within [1, 400] μs of a preceding event or muon-veto time window, the DC was excluded (this requirement was also applied to singles). The fraction of DAQ time remaining for IBD analysis after implementing these multiple-coincidence criteria was about 98.4% for each AD, and is reported as ε_m in Table II. This multiplicity selection efficiency was derived as described in Ref. [47], and calculated using the duration of the coincidence time window $T_c = 399$ μs and the rate of uncorrelated single events R_s (which are uncorrelated events that satisfy the criteria of Sections IV.2.1-IV.2.3; not singles,

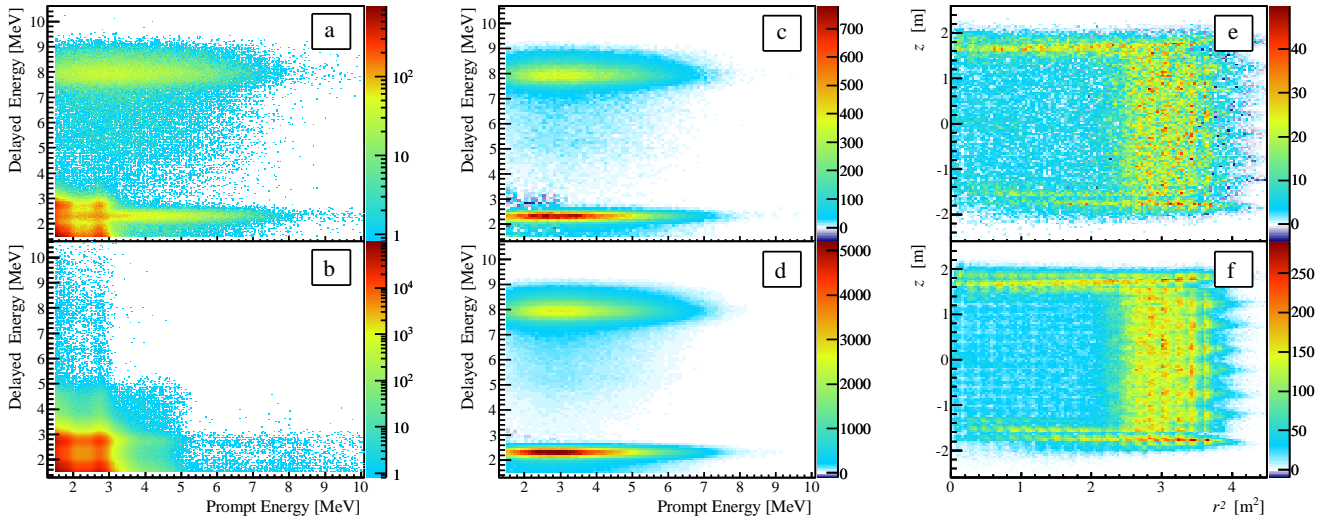


FIG. 2. (a) Distribution of prompt *vs.* delayed reconstructed energy for all double coincidences with a maximum 50-cm separation in all near-hall ADs, (b) total (621-day) accidental background sample (ABS) for all ADs in the near halls, (c) and (d) are the distributions of prompt *vs.* delayed reconstructed energy after subtracting the total ABS for the far and near halls, respectively, (e) and (f) are the reconstructed positions of all prompt events after subtracting the total ABS for the far and near halls, respectively. The sparser distribution of events at the bottoms of the ADs is due to the presence of acrylic supports below the IAV.

which exclude events involved in coincidences):

$$\varepsilon_m = e^{-R_s T_c} \left\{ e^{-(R_s + R_\mu) T_c} + \frac{R_\mu}{R_s + R_\mu} [1 - e^{-(R_s + R_\mu) T_c}] + \frac{R_s}{R_s + R_\mu} e^{-R_\mu T_c} [1 - e^{-(R_s + R_\mu) T_c}] - \frac{R_s}{2R_s + R_\mu} e^{-R_\mu T_c} [1 - e^{-(2R_s + R_\mu) T_c}] \right\}. \quad (5)$$

IV.2.5. Coincidence Distance

The set of DCs was largely comprised of accidental coincidences (whose positions are uncorrelated throughout the detector); therefore, the spatial separation of the reconstructed positions of the prompt and delayed events d_c was required to be within 50 cm. This rejected 98% of the accidental coincidences at a loss of 25% of the IBDs.

Figure 2(a) shows the distribution of prompt energy *vs.* delayed energy for all DCs in all near-hall ADs after applying the coincidence-distance criterion. Bands for both the 2.22-MeV $n\text{H}$ and 8-MeV $n\text{Gd}$ delayed events are apparent, with a large background of low-energy DCs around the $n\text{H}$ band. The clusters around 1.5 and 2.7 MeV are due to γ 's from ^{40}K and ^{208}Tl decays, respectively. The bands between these clusters are dominated by the decay products of ^{238}U . The measured $n\text{H}$ γ energy was around 2.33 MeV, which is offset from the

true value of 2.22 MeV because of nonlinear detector response and the calibration of the energy scale with $n\text{Gd}$ events. The $n\text{H}$ delayed events were fit as described in Section VII.3, providing a mean and a standard deviation σ for each AD. Delayed events were required to have E_{rec} within 3σ (≈ 0.42 MeV) of the mean for each AD, which excludes γ 's from ^{40}K . The accidental background from the remaining decays was effectively removed by the subtraction described in Section V. Backgrounds from correlated events are described in Section VI. Efficiencies and uncertainties of the IBD selection criteria are described in Section VII.

V. ACCIDENTAL BACKGROUND

Accidental backgrounds were caused by two uncorrelated AD events that satisfied the IBD selection criteria, and were almost entirely due to natural radioactivity in the materials around and within the detectors. The energy spectra of this background are visible below 3 MeV in Fig. 2(a). Because the delayed event of an $n\text{H}$ IBD is from a 2.22-MeV γ , which overlaps with this background spectrum, the accidental background rate relative to the IBD rate was typically > 50 times that of the $n\text{Gd}$ -IBD analysis for the ADs in EH3 after applying all IBD selection criteria.

The background was estimated for each AD within each run (about 2-3 days) by constructing accidental background samples (ABSs) from the singles in a run. An ABS was constructed by sequentially pairing singles from the first half of the run with singles from the second

half of the run. The resulting ABS consisted of $N_{\text{ABS-tot}}$ accidentals, and after applying the remaining IBD selection criteria (distance and energy), the ABS consisted of $N_{\text{ABS-cut}}$ accidentals. To obtain the true value for $\varepsilon_{\text{ABS}} \equiv N_{\text{ABS-cut}}/N_{\text{ABS-tot}}$, the calculation of ε_{ABS} was repeated for several hundred different pairing sequences of the singles, and the Gaussian mean of the resulting distribution was taken as ε_{ABS} . Figure 2(a) shows the energy distribution of all DCs (621 days) of all near-hall ADs without applying the delayed-energy criterion, and Fig. 2(b) shows the energy distribution of the total ABS (621 days) of all near-hall ADs after applying the coincidence-distance criterion. Each ABS was scaled to a calculated number of accidentals (N_{Acc}) and subtracted from its corresponding number of DCs (N_{DC}) to obtain the energy distribution of correlated DCs (N_{Cor}), which are dominantly due to IBDs:

$$\begin{aligned} N_{\text{Cor}} &= N_{\text{DC}} - N_{\text{Acc}}, \\ N_{\text{Acc}} &\equiv R_{\text{Acc}} \cdot T_{\text{DAQ}} \cdot \varepsilon_{\mu} \cdot \varepsilon_{\text{ABS}}, \end{aligned} \quad (6)$$

where T_{DAQ} is the DAQ time, ε_{μ} is the muon-veto efficiency, and R_{Acc} is the rate of coincidence of uncorrelated single events, which is expressed as [47]

$$\begin{aligned} R_{\text{Acc}} &= R_s^2 \cdot T_c \cdot \varepsilon_m \\ &\approx R_s \cdot e^{-R_s T_c} \cdot R_s T_c e^{-R_s T_c}, \end{aligned} \quad (7)$$

where R_s is the rate of uncorrelated single events and ε_m is the multiplicity selection efficiency, both defined in Eq. (5). The approximation of Eq. (5) used in the second line ($\varepsilon_m \approx e^{-R_s T_c} \cdot e^{-R_s T_c}$) results from the condition $(R_s + R_{\mu})T_c \ll 1$ and is valid to within 0.1% for $T_c = 399 \mu\text{s}$, $R_s = 20 \text{ Hz}$, and the R_{μ} in Table II. This approximation is not used in this analysis, but is shown here to illustrate the basic components of the calculation: $e^{-R_s T_c}$ is the probability of no prior event within T_c and $R_s T_c e^{-R_s T_c}$ is the probability of a subsequent event within T_c . N_{DC} , N_{Acc} , and N_{Cor} are listed for each AD in Table II.

Figure 2(d) shows the energy distribution of N_{Cor} for all near-hall ADs [Fig. 2(c) shows N_{Cor} for the far-hall ADs], where the $n\text{H}$ γ peak is clearly isolated from the accidental-dominated DCs shown in Fig. 2(a). The effectiveness of the subtraction is also illustrated in Fig. 3, which shows the energy spectrum of the delayed events after subtracting the accidental background for all near-hall ADs and all far-hall ADs. Both the $n\text{H}$ and $n\text{Gd}$ peaks are very similar between the two groups of ADs. Figures 2(e) and 2(f) show the reconstructed positions of N_{Cor} prompt events after subtracting the accidental background for all ADs in the far and near halls, respectively. The positions are generally uniform throughout the GdLS and LS volumes. The smaller concentration of events in the GdLS volume ($r^2 < 2.40 \text{ m}^2$ and $|z| < 1.50 \text{ m}$) is due to the greater fraction of neutron-captures on Gd.

The uncertainty of N_{Cor} is composed of the statistical uncertainties of N_{DC} and $N_{\text{ABS-cut}}$, and the systematic

uncertainty of R_{Acc} , which is determined by the uncertainty of R_s . The uncertainty from ε_m was negligible: using Eq. (5) and $R_s = 40 \text{ Hz}$, $R_{\mu} = 200 \text{ Hz}$, and $T_c = 399 \mu\text{s}$ (which are conditions similar to those in EH1), $d\varepsilon_m = 3 \times 10^{-6} dR_{\mu} - 6 \times 10^{-3} dR_s$. By taking the average over a run, the induced systematic uncertainty from variations in R_s or R_{μ} was negligible.

R_s was estimated as the average of an upper and lower limit. The upper limit was derived from the total number of AD events after applying muon-event vetoes. These events were dominantly singles but included DCs and multiple coincidences. The lower limit was derived from the number of singles plus DCs that did not satisfy the coincidence-distance criterion. These DCs were dominantly accidentals. Time-averaged values of R_s are listed in Table II for each AD. The difference between the two limits was assigned as the systematic uncertainty of R_s and propagated to R_{Acc} , resulting in 0.18%, 0.16% and 0.05% uncertainties of the accidental rate in EH1, EH2, and EH3, respectively. The larger uncertainties for the near halls are due to the higher rates of IBD reactions from reactor antineutrinos, which enlarged the upper limits. Figure 4 shows R_s as a function of time for each AD, where a downward trend began after the water shields were filled. During the first few weeks, R_s decreased by $< 0.05 \text{ Hz per day}$ for near-hall ADs and by $< 0.08 \text{ Hz per day}$ for far-hall ADs. The near-hall water shields were filled earlier and so, the AD rates stabilized earlier. Considering that R_s was calculated every 2-3 days, the uncertainty introduced to R_{Acc} by these trends was estimated to be $< 2 \times 10^{-5}$, which is more than an order of magnitude smaller than the uncertainty in EH3. There were also instantaneous increases of R_s , which were caused by

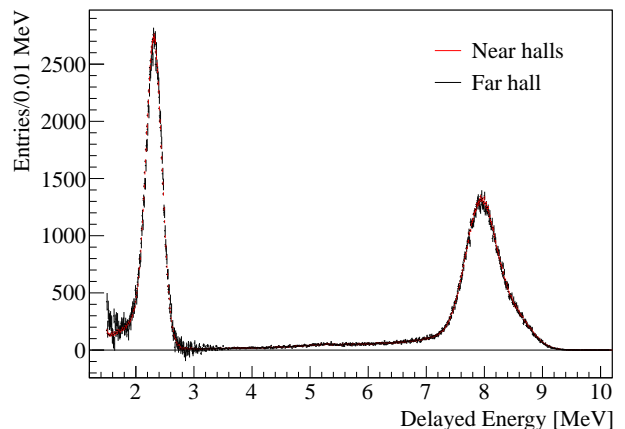


FIG. 3. Reconstructed delayed-energy distribution after subtracting the accidental background for all four ADs in EH3 (black) and all four ADs in EH1 and EH2 (red), where the far-hall spectrum has been normalized to the area of the near-halls spectrum. (621 days of data.)

muon-generated spallation products such as ${}^9\text{Li}$ and ${}^8\text{He}$ (Section VI.1), and spallation neutrons (Section VI.2). From a study of R_s vs. time after muon-event vetoes, the impact of these products was estimated to be negligible.

Two methods were used to validate the subtraction of the accidental background. The first method used the distribution of distance between the prompt and delayed events, which was dominated by accidental coincidences at large separations. After subtracting the accidental background, the resulting number of correlated DCs with large separations is expected to be zero. Figure 5 shows the distribution of distance between the prompt and delayed events for DCs, accidentals, and correlated DCs. The two upper panels of Fig. 5 contain calculations of the relative difference between the measured number of double coincidences (N_{DC}) and the predicted number of accidentals (N_{Acc}), beyond 200 cm. These differences are consistent with zero with respect to their statistical uncertainties. A constant fit in the bottom panel also shows that the distribution of selected $n\text{H}$ IBD candidates (N_{Cor}) beyond 200 cm is consistent with an expected fraction of about 0.05%, which was determined from Monte Carlo simulation. This fraction corresponds to an expected fitted constant of about 0 (3) entries/2 cm for the far (near) hall(s).

The subtraction of the accidental background was also validated by the distribution of time between prompt and delayed events. Figure 6 shows the distribution of time between prompt and delayed events for DCs, accidentals, and correlated DCs. The two upper panels of Fig. 6 contain calculations of the relative difference between the measured number of double coincidences (N_{DC}) and the predicted number of accidentals (N_{Acc}), beyond 1000 μs .

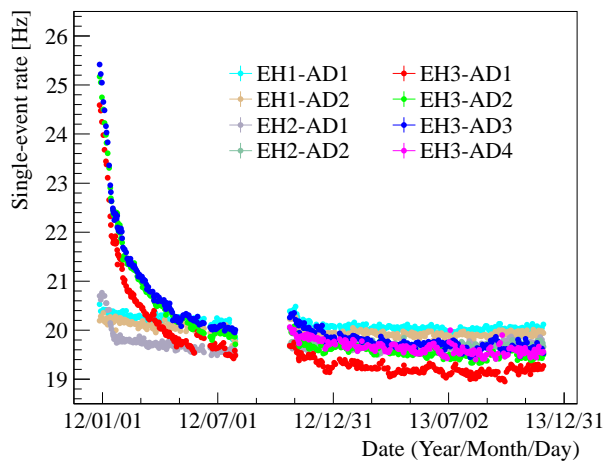


FIG. 4. Rate of uncorrelated single events vs. time for each AD. Rates stabilized several months after water shields were filled (EH3 was filled less than a month before data-recording began).

These differences are consistent with zero with respect to their statistical uncertainties. A constant fit in the bottom panel also shows that the distribution of selected $n\text{H}$ IBD candidates (N_{Cor}) beyond 1000 μs is consistent with an expected fraction of 0.7%, which was determined from Monte Carlo simulation. This fraction corresponds to an expected fitted constant of about 16 (110) entries/10 μs for the far (near) hall(s).

VI. CORRELATED BACKGROUNDS

After the accidental background was subtracted to obtain N_{Cor} , correlated backgrounds were subtracted to obtain the number of measured $n\text{H}$ IBDs (N_{IBD}). In EH3 (EH1), $N_{\text{IBD}}/N_{\text{Cor}} = 99.2\%$ (99.0%). Correlated backgrounds consist of prompt and delayed events that originate from a single source and satisfy the IBD selection criteria. These backgrounds are primarily from cosmogenic muon-induced ${}^9\text{Li}/{}^8\text{He}$ isotopes and spallation neutrons, and neutrons from ${}^{241}\text{Am}$ - ${}^{13}\text{C}$ calibration

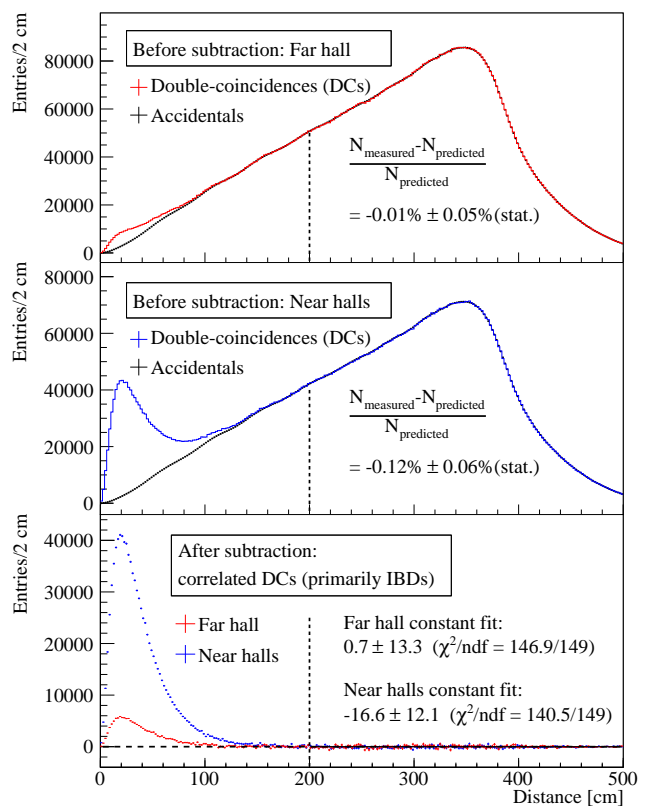


FIG. 5. Distributions of the distance between the prompt and delayed events of all measured double coincidences and of the predicted accidental backgrounds (black points) in the far hall (top panel) and near halls (middle panel). The bottom panel shows the distance distributions after subtracting the accidental backgrounds for the near halls (blue) and the far hall (red). See the text for details.

sources interacting with the SSV and its appendages. The $^{13}\text{C}(\alpha,n)^{16}\text{O}$ background is less significant for the $n\text{H-IBD}$ analysis than for the $n\text{Gd-IBD}$ analysis and is briefly discussed.

VI.1. $^9\text{Li}/^8\text{He}$ Background

Cosmogenic muons and their spallation products interact with the ^{12}C in organic liquid scintillators, producing neutrons and isotopes via hadronic or electromagnetic processes. Among the muon-induced isotopes, ^9Li and ^8He β^- -decay to neutron-unstable excited states, immediately followed by the ejection of a neutron. These β^- -neutron decays mimic the prompt and delayed events of IBD reactions. The lifetimes of ^9Li and ^8He (257.2 and 171.7 ms, respectively) are longer than the muon-veto windows for a μ_{WS} or μ_{AD} (see Section IV.2), leading to a contamination of the IBD candidate sample. The temporal relation between $^9\text{Li}/^8\text{He}$ decays and prior detected muons was used to estimate the collective yield of

the ^9Li and ^8He background $N_{\text{Li/He}}$ in each hall. The distribution of the time between the prompt event of a DC and its preceding muon was described by a formula following Ref. [48]:

$$N(t) = N_{\text{Li/He}} \left[r \cdot \lambda_{\text{Li}} \cdot e^{-\lambda_{\text{Li}}t} + (1-r) \cdot \lambda_{\text{He}} \cdot e^{-\lambda_{\text{He}}t} \right] + N_{\text{BB}} \cdot \lambda_{\text{BB}} \cdot e^{-\lambda_{\text{BB}}t} + N_{\text{DC}\mu} \cdot R_{\mu} \cdot e^{-R_{\mu}t}, \quad (8)$$

where $\lambda_{\text{isotope}} \equiv R_{\mu} + 1/\tau_{\text{isotope}}$ and τ_{isotope} is the lifetime of the specific isotope (^9Li or ^8He), R_{μ} is the muon rate (which depends on the muon selection criteria), r is the fraction of ^9Li decays among the ^9Li and ^8He decays, $\lambda_{\text{BB}} \equiv R_{\mu} + 2/\tau_{\text{B}}$, and N_{BB} and $N_{\text{DC}\mu}$ are the numbers of ^{12}B - ^{12}B coincidences and all other double coincidences (excluding those from cosmogenically-produced isotopes), respectively.

The beta-decaying isotope ^{12}B was produced with a yield about one order of magnitude greater than the combined yield of ^9Li and ^8He . With its lifetime of $\tau_{\text{B}} \approx 29$ ms, double coincidences of ^{12}B - ^{12}B originating from a single muon contributed mainly within the first ≈ 50 ms of the time since the preceding muon distribution. The fitted value of $N_{\text{Li/He}}$ changed by up to 10% when including and excluding the ^{12}B term.

The fraction of ^9Li r could not be reliably determined because of the similar lifetimes of ^9Li and ^8He . Measurements of ^9Li and ^8He yields from Ref. [49] indicate that r should be between roughly 85% and 100% at Daya Bay. Varying r in this range resulted in a 4% variation in the fitted value of $N_{\text{Li/He}}$ in all halls.

To obtain a better estimate of $N_{\text{Li/He}}$, $N_{\text{DC}\mu}$ was reduced by suppressing accidentals among the double coincidences. This was done by augmenting the prompt-energy criterion from $1.5 < E_p < 12.0$ MeV to $3.5 < E_p < 12.0$ MeV. The measured number of $^9\text{Li}/^8\text{He}$ was corrected with the efficiency of the augmented criterion with respect to the nominal criterion. This ratio was determined to be 74% by averaging measurements from all three halls with visible muon energy $E_{\mu}^{\text{vis}} > 1$ GeV (E_{μ}^{vis} is the detected energy that was deposited by a muon traversing the detector). The weighted average of the three measurements had a statistical uncertainty of 5%. The systematic uncertainty was estimated as the difference between the average and a Monte Carlo simulation, and therefore accounted for backgrounds in the measurements. The simulation used β spectra of $^9\text{Li}/^8\text{He}$ decays calculated as those in Ref. [50]. The resulting prompt-energy spectrum from the simulation is shown in Fig. 11, where it has been normalized to $N_{\text{Li/He}}$. The difference in efficiency between the measurement and simulation was 6%, giving a total uncertainty of 8% for the efficiency of the augmented E_p criterion.

The $^9\text{Li}/^8\text{He}$ background was determined for three ranges of E_{μ}^{vis} : 0.02-1.0 GeV, 1.0-2.5 GeV, and > 2.5 GeV. The highest energy range was defined as such because it identically defines a μ_{sh} , which was vetoed for

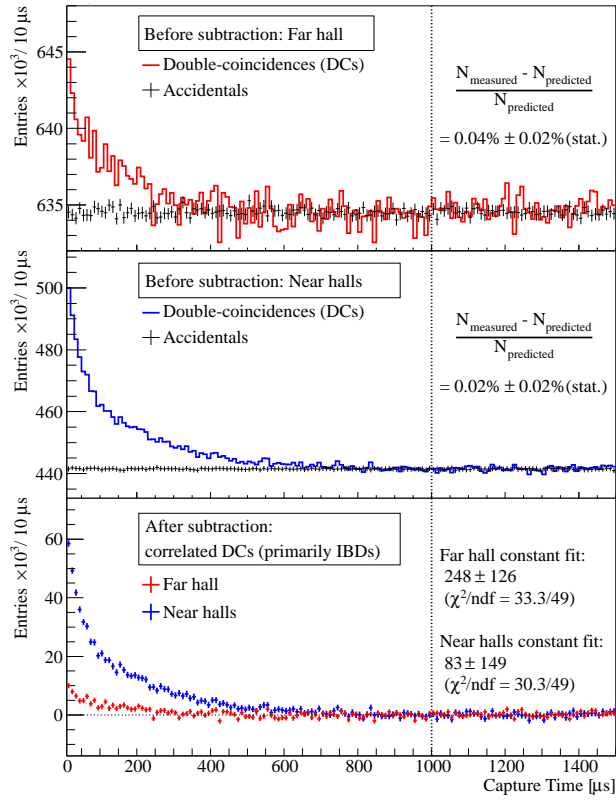


FIG. 6. Distributions of the time between the prompt and delayed events of all measured double coincidences and of the predicted accidental backgrounds (black points) in the far hall (top panel) and near halls (middle panel). The bottom panel shows the time distributions after subtracting the accidental backgrounds for the near halls (blue) and the far hall (red). See the text for details.

1 s (see Table I) and therefore contributed only $O(1)\%$ of the total ${}^9\text{Li}/{}^8\text{He}$ background. The lowest energy range was defined as such because it could not provide a reliable fit of ${}^9\text{Li}/{}^8\text{He}$ due to its higher R_μ and lower signal-to-background ratio: relative to the middle energy range, R_μ was 14 (11) times greater and $N_{\text{Li}/\text{He}}/N_{\text{DC}\mu}$ was about 5 (10) times lower, in EH1 (EH3).

To obtain a more reliable estimate of the ${}^9\text{Li}/{}^8\text{He}$ background of the lowest energy range, R_μ was reduced and the signal-to-background ratio was increased, by isolating the muons that produced ${}^9\text{Li}/{}^8\text{He}$. Under the assumption that the isotopes were produced along with neutrons, every μ_{AD} without a subsequent neutron (defined as a 1.8-12 MeV event within 20-200 μs) was excluded. The measured number of ${}^9\text{Li}/{}^8\text{He}$ was corrected with the efficiency of this altered μ_{AD} definition with respect to the nominal definition. Since this ratio could not be determined for the lowest energy range, the ratio for the middle energy range was used as a proxy. This ratio was determined to be about 69% (66%) in the far (near) hall(s). A 100% uncertainty was assigned to the background for the lowest energy range, corresponding to a 1σ lower bound of 35% (33%) for the efficiency of the altered μ_{AD} definition in the far (near) hall(s).

The number of ${}^9\text{Li}/{}^8\text{He}$ for both the middle and lowest energy ranges in EH1 and EH2 were determined with the combined data samples of EH1 and EH2. The energy spectra of muons in EH1 and EH2 are similar [30] such that their yields of ${}^9\text{Li}/{}^8\text{He}$ per muon are expected to agree to $O(1)\%$ [51, 52]. The E_μ^{vis} spectra of the two near halls were observed to differ in scale by about 7%. This was due to a 7% lower average gain of the high-charge range [53] of the EH2 electronics. After scaling the E_μ^{vis} spectrum of EH2 by 7%, the difference between the near-hall spectra was $O(1)\%$ across the two energy ranges. This scaling introduced a negligible uncertainty to the fitted number of ${}^9\text{Li}/{}^8\text{He}$. The muon rate R_μ of the combined fit was fixed to the DC-weighted average of the measured muon rates in the two near halls. Combining the uncertainties of the measured muon rates (0.3%) and numbers of DCs (1%), the weighted average had a 0.2% uncertainty. This 0.2% uncertainty of R_μ corresponded to a 27% change in the number of ${}^9\text{Li}/{}^8\text{He}$ via Eq. (8) for the middle energy range. The 0.2% uncertainty had a negligible impact on the lowest energy range because its muon rate was reduced as described above. The fitted number of ${}^9\text{Li}/{}^8\text{He}$ was divided among the near halls according to their measured muon rates (after scaling EH2) multiplied by their DAQ times.

Examples of fits to the time since the preceding muon without the ${}^{12}\text{B}$ term for $E_\mu^{\text{vis}} > 1.0$ GeV are shown in Fig. 7. The green areas represent the non-cosmogenic DCs and the red areas represent the ${}^9\text{Li}/{}^8\text{He}$ DCs. For presentation purposes, the plots use wider bins than the actual fits.

Uncertainties were from statistics, the ${}^9\text{Li}$ fraction r , the contribution of ${}^{12}\text{B}$, the augmented E_p selection criterion, the altered μ_{AD} definition for the lowest energy

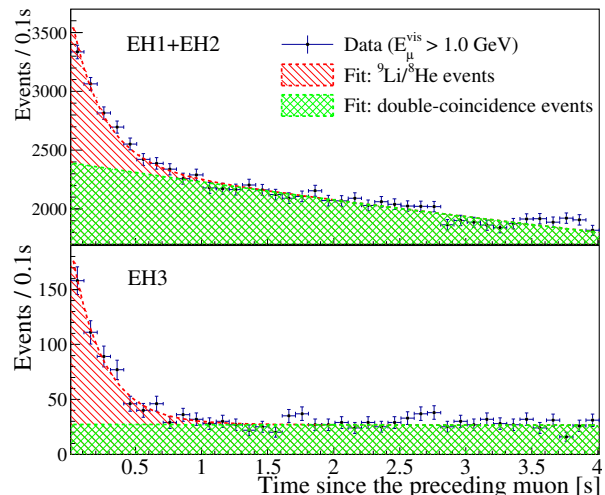


FIG. 7. Examples of fits of the time since the preceding muon in EH1+EH2 (top) and EH3 (bottom) for $E_\mu^{\text{vis}} > 1.0$ GeV. The green area is the non-cosmogenic double-coincidence component and the red area is the ${}^9\text{Li}/{}^8\text{He}$ component.

range, and binning effects. The total uncertainty of the ${}^9\text{Li}/{}^8\text{He}$ background was determined from the combination of all components of uncertainty, and was dominated by statistical uncertainty.

Table II lists the determined rate of background DCs due to ${}^9\text{Li}/{}^8\text{He}$ in each hall. The rate was calculated by dividing the estimated $N_{\text{Li}/\text{He}}$ by $T_{\text{DAQ}}\epsilon_\mu\epsilon_m$ and correcting for the efficiencies of the altered definitions of the E_p and μ_{AD} criteria.

Since the $n\text{H}$ - and $n\text{Gd}$ -IBD analyses used different data samples, and the efficiencies were determined with distinct methods, there was no correlation of the ${}^9\text{Li}/{}^8\text{He}$ background determinations between the $n\text{H}$ - and $n\text{Gd}$ -IBD analyses.

VI.2. Fast-neutron Background

In addition to producing radioactive isotopes such as ${}^9\text{Li}$ and ${}^8\text{He}$, cosmogenic muon interactions can generate energetic neutrons via spallation. Upon reaching an AD, a neutron may scatter off a proton and then capture on hydrogen, creating a prompt-delayed coincidence. Given the high efficiency with which μ_{WGS} 's are detected, the neutrons that contribute to this background predominantly originate from the rock surrounding an OWS. Because the LS volume is more accessible than the GdLS volume to the externally-produced neutrons, this background is significantly higher than for the $n\text{Gd}$ -IBD analysis.

A Monte Carlo simulation of neutrons induced from muons in the water shields was performed. An empirical parameterization for neutron production from cosmogenic muons [54] and the estimated average muon energy

in an experimental hall [30] were used to generate the initial kinetic energy and zenith angle distributions of the neutrons. The resulting prompt-energy spectra of the simulated neutrons are shown in Fig. 8. The increase of events with decrease of energy in the LS volume is due to the lesser containment of the recoil protons within the LS volume: the protons that recoil from fast neutrons that capture in the LS volume are closer to the boundary of the scintillating region compared to those associated with fast neutrons that capture in the GdLS volume, and thus, are more likely to deposit less energy in scintillator.

To determine the fast neutron background spectrum, a sample of spallation neutrons was obtained by slightly modifying the nominal IBD selection criteria: the upper prompt-energy criterion was removed and the OWS muon-event veto was excluded. Muons identified with the IWS were still vetoed to avoid confusing a spallation neutron with a muon event in an AD. In addition, the prompt event was required to occur within 300 ns after an OWS-identified muon and the delayed event at least 15 μ s after the muon to exclude muon decays. The OWS-identified muon events were required to occur at least 1200 μ s after any muon events in an AD or the IWS. The prompt recoil-energy spectrum of the OWS-identified spallation neutrons from EH1 is shown in Fig. 9. Figure 9 also shows the prompt-energy distribution of IBD candidates without the upper E_p criterion and the spectrum obtained from the simulation. The OWS-identified and simulated spectra were normalized to the IBD candidates above 12 MeV, revealing consistent shapes.

Plotting the prompt recoil-energy spectrum in a log-log scale (see the inset of Fig. 9) shows that the low-energy portion of the spectrum up to several tens of MeV is consistent with a power law [$N(E) = N_0 E^{-a}$], while there is a distinct energy-dependence at higher energies. The entire spectrum could be fit after adding one degree of

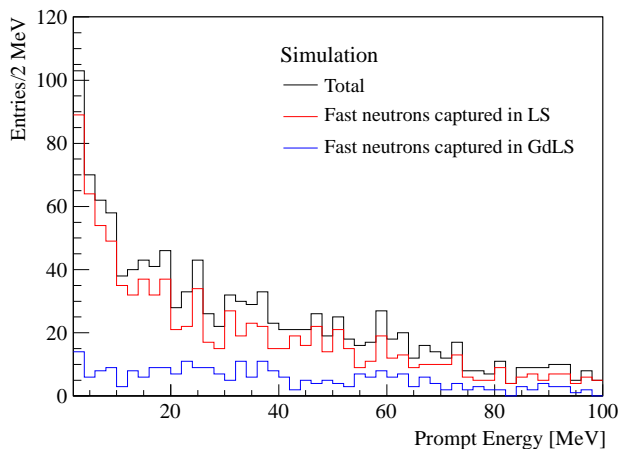


FIG. 8. Simulated prompt-recoil-energy spectra of spallation neutrons produced in the IWS or OWS by cosmogenic muons. See text for details.

freedom to the power law; namely, extending the exponent to have a first-order dependence on energy:

$$N(E) = N_0 \left(\frac{E}{E_0} \right)^{-a - \frac{E}{E_0}}. \quad (9)$$

The fit of Eq. (9) resulted in a χ^2 per degree of freedom close to 1 for each hall. Bin widths of 2 MeV were selected for the near halls based on the stability of the fit parameters and the χ^2 per degree of freedom. Due to the lower statistics of EH3, the corresponding bin width was 3 MeV. The value of a was consistent among the three halls, yielding an average of 0.690 ± 0.023 . The value of E_0 averaged to (101.7 ± 2.1) MeV for the near halls and was (110 ± 10) MeV for the far hall.

The fast neutron background and its uncertainty were both estimated as in Ref. [12]. The background was estimated as the number of events within the nominal prompt-energy selection window ($1.5 < E_{\text{rec}} < 12$ MeV) in the normalized OWS-identified spectrum of each hall. The spectrum was normalized to the extended IBD spectrum from all the ADs in a hall, between 12 and 300 MeV. The systematic uncertainty was estimated using both the OWS-identified and extended IBD spectra. First, the extended IBD spectrum of each hall was fit between 12 and 300 MeV with the power law given in Eq. (9). Then, the difference was taken between the integral of the function and the number of events in the normalized OWS-identified spectrum, with E_{rec} between 1.5 and 12 MeV. The largest relative difference among the three halls (6% in EH3) was assigned to be the systematic uncertainty

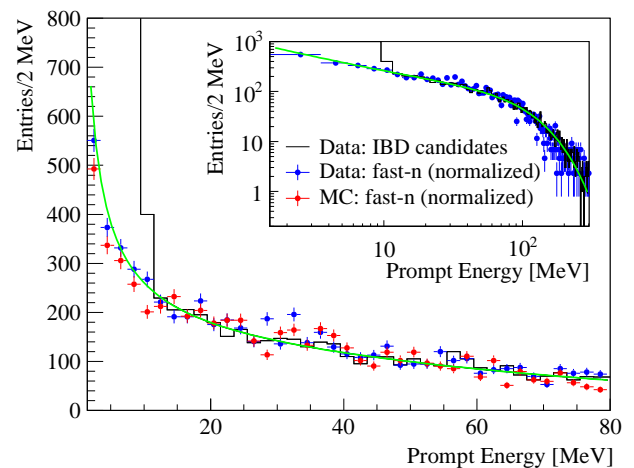


FIG. 9. Reconstructed prompt recoil-energy spectra of fast spallation neutrons from IBD candidates in EH1 with the upper E_p limit removed (black line), OWS-identified muons (blue points), and simulation (red points). The latter two spectra were normalized to the area of the extended IBD spectrum. The green curve is the fit of the extended IBD spectrum using a first-order power law (see the text). The inset is a log-log scaling of the plot.

for each hall. In addition, each hall had a distinct fit uncertainty, which included the statistical uncertainty and was about 6%, 7%, and 18% for EH1, EH2, and EH3, respectively. The results are listed for each experimental hall in Table II.

There was no significant correlation between the n H- and n Gd-IBD fast neutron analyses because of their different selection criteria and independent event samples.

VI.3. Am-C Calibration Source Background

One of the calibration sources deployed from each of the three ACUs atop an AD was an ^{241}Am - ^{13}C neutron source with a detected rate of 0.7 Hz [55]. Neutrons from these sources could inelastically scatter with the nuclei in the surrounding steel (SSV, ACU enclosures, *etc.*) and then capture on Fe, Cr, Ni, or Mn within the steel, producing γ 's that could enter the scintillating regions and satisfy the IBD selection criteria. During the pause to install the final two ADs in the summer of 2012, two of the three Am-C sources were removed (from ACU-B and -C) from each AD in EH3, reducing this background in EH3 by about 40% relative to the previous analysis [15].

This background was estimated using a special Am-C source [56] whose neutron emission rate was approximately 80 times higher than the Am-C calibration sources. The special source was positioned on the top of EH3-AD2 near ACU-B for about 10 days during the summer of 2012. Figure 10 shows the resulting distribution of the reconstructed vertical position of delayed events, which exhibits an excess at positive z (the top half of the AD). For comparison, the distribution from the adjacent EH3-AD1 (which had only an Am-C calibration source in ACU-A) is shown over the same period, exhibiting no apparent asymmetry. The distributions of the vertical position of prompt events are similar.

The number of background DCs from the special Am-C source N_{Special} was estimated by subtracting N_{DC} of EH3-AD1 from N_{DC} of EH3-AD2 during the same period, resulting in $N_{\text{Special}} = 137 \pm 41.6$. The vertical positions of both the prompt and delayed events were required to be in the top half of each AD ($z_p > 0$ and $z_d > 0$).

The intensity of the special Am-C source was scaled to the intensities of the Am-C calibration sources of each AD using “delayed-type” events, which are defined as singles that satisfy the delayed-energy criterion. The relatively low energy of the n H γ selection admitted significant radioactive contamination into this sample of events. To avoid this contamination, the higher-energy n Gd delayed-type events were used. In Ref. [56], the number of n Gd delayed-type events due to an Am-C source $[N_{\text{AmC-dtype}}]_{n\text{Gd}}$ was estimated by the asymmetry of the vertical position distribution, which was similar to that in Fig. 10. The number of background DCs from

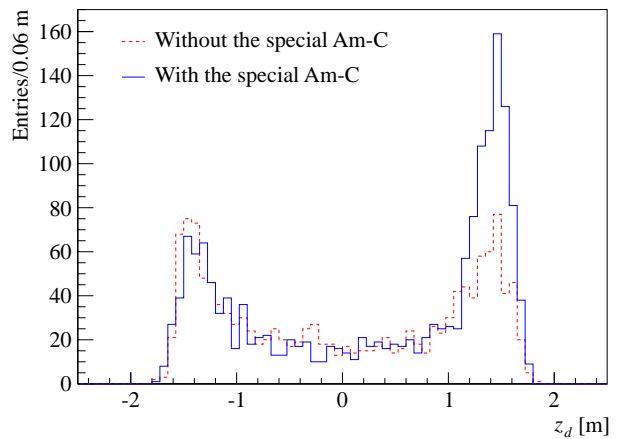


FIG. 10. Distribution of vertical position of delayed events for EH3-AD2 with both its Am-C calibration source and the special Am-C source (solid blue line), and EH3-AD1 with only its Am-C calibration source (dashed red line). All sources were located at the tops of the detectors: $z \approx 2.5$ m.

each Am-C calibration source N_{AmC} was estimated as

$$N_{\text{AmC}} = N_{\text{Special}} \left[\frac{N_{\text{AmC-dtype}}}{N_{\text{Special-dtype}}} \right]_{n\text{Gd}}, \quad (10)$$

where $N_{\text{AmC-dtype}}$ is counted over the entire 621-day data period. The n Gd ratio in Eq. (10) was about 0.12 for the far hall and 0.23 for the near halls. The uncertainty of N_{AmC} was comprised of the 30% statistical uncertainty of N_{Special} and an approximate 40% systematic uncertainty shared with the n Gd-IBD analysis from a difference in delayed-type event rates among the near- and far-hall ADs. This gives a total uncertainty of 50% for the Am-C background. Table II lists the rate of Am-C background DCs, which is N_{AmC} divided by $T_{\text{DAQ}}\varepsilon_{\mu}\varepsilon_m$, for each AD. The prompt-energy spectrum of the Am-C background was modeled with an exponential, which was determined from both the simulation and the data with the special Am-C source. The spectrum is shown in Fig. 11.

For the n Gd-IBD analysis, this background had a 45% total uncertainty. Considering the common 40% systematic uncertainty, the Am-C background determination was found to have a correlation coefficient of about 0.7 between the n H- and n Gd-IBD analyses:

$$\frac{40\% \cdot 40\%}{50\% \cdot 45\%} = 0.7. \quad (11)$$

VI.4. $^{13}\text{C}(\alpha, n)^{16}\text{O}$ Background

The $^{13}\text{C}(\alpha, n)^{16}\text{O}$ background is from four dominant sources of alpha decays in the liquid scintillator: the ^{227}Ac (in the GdLS), ^{238}U , and ^{232}Th decay chains and

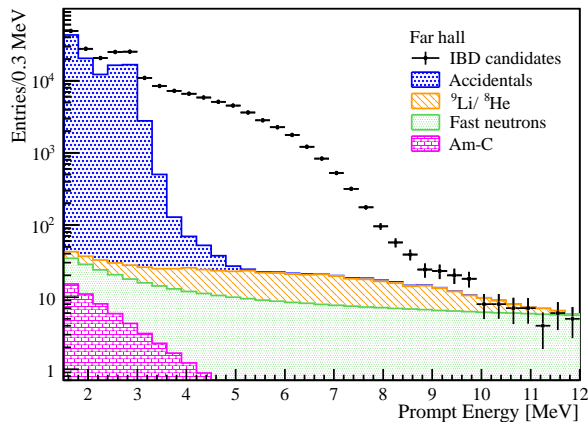


FIG. 11. Reconstructed prompt-energy distributions of the measured double coincidences after IBD selection (black points) and estimated backgrounds, for the sum of all ADs in EH3.

^{210}Po , which is produced in the decay of ^{222}Rn . The (α, n) background rate was roughly estimated using the rates from the $n\text{Gd}$ -IBD analysis [12] and the ratio of the $n\text{H}/n\text{Gd}$ IBD selection efficiencies. The estimate in EH3 was approximately 0.02 ± 0.01 DCs per AD per day. This estimate is expected to be conservative because of the lower activity of the LS relative to the GdLS: using the selection criteria outlined in Ref. [45], the concentration of ^{232}Th was determined to be a few hundred times greater in the GdLS while that of ^{238}U was estimated to be similar. The uncertainty of the $^{13}\text{C}(\alpha, n)^{16}\text{O}$ background contributed negligibly to the total uncertainty of $\sin^2 2\theta_{13}$ (see Table IV) and therefore, this background was neglected in this analysis.

VI.5. Summary of Correlated Backgrounds

The rates of the correlated backgrounds are summarized in Table II and their prompt-energy distributions are illustrated in Fig. 11 for EH3. The rates of $n\text{H}$ IBDs after subtracting all the backgrounds are listed for each AD in Table II.

With respect to the previous $n\text{H}$ -IBD analysis [15], the absolute uncertainty of the dominant $^9\text{Li}/^8\text{He}$ background was reduced by about 30% because of increased statistics and various improvements in the method. Reductions in the uncertainties of the fast neutron and Am-C backgrounds resulted primarily from an improved method of estimation and a fit of the full spectrum, and the removal of some Am-C sources, respectively. The overall uncertainty of backgrounds was reduced by 30%.

Comparing to the $n\text{Gd}$ -IBD analysis, the fast neutron background was about four to five times larger relative to the IBD rate in EH3, while the $^9\text{Li}/^8\text{He}$ and ^{241}Am -

^{13}C backgrounds were equal within uncertainties, and the $^{13}\text{C}(\alpha, n)^{16}\text{O}$ background was about half as large. The absolute uncertainty of the fast neutron background was about four to five times larger relative to the IBD rate in EH3, while the uncertainties of the $^9\text{Li}/^8\text{He}$ and ^{241}Am - ^{13}C backgrounds were similar, and the uncertainty of the $^{13}\text{C}(\alpha, n)^{16}\text{O}$ background was about half that of the $n\text{Gd}$ -IBD analysis. The impact of the uncertainties of the background estimations on the uncertainty of $\sin^2 2\theta_{13}$ is described at the end of Section VIII.2.

Due to the sharing of uncertainty components between the $n\text{Gd}$ - and $n\text{H}$ -IBD analyses, the Am-C background determinations had a correlation coefficient of about 0.7, while the $^9\text{Li}/^8\text{He}$ and fast neutron background determinations were uncorrelated, and the $^{13}\text{C}(\alpha, n)^{16}\text{O}$ background was neglected in this analysis.

VII. DETECTION EFFICIENCY

The expected number of selected IBDs from one AD was determined according to Eq. (1), in which the efficiency-weighted number of target protons was calculated considering antineutrino interactions in the GdLS, LS, and acrylic volumes v :

$$N_\varepsilon = \varepsilon_\mu \varepsilon_m \left[\sum_v^{\text{GdLS, LS, acry.}} N_{p,v} \varepsilon_{E_p, v} \varepsilon_{T, v} \varepsilon_{E_d, v} \right] \varepsilon_D, \quad (12)$$

where ε_μ and ε_m are the muon-veto and multiplicity selection efficiencies of the AD, N_p is the number of target protons of the AD, ε_{E_p} and ε_{E_d} are the prompt- and delayed-energy selection efficiencies, and ε_T and ε_D are the coincidence-time and -distance selection efficiencies, respectively. The PMT flash selection efficiency (Section IV.2.1) is not included due to its negligible inefficiency.

The number of target protons was determined for each AD from measurements made prior to AD deployment. The muon-veto, multiplicity, and distance selection efficiencies were determined with data. The prompt- and delayed-energy, and time selection efficiencies were determined with a simulation using a predicted antineutrino spectrum such as described in Section III. The simulation framework of Daya Bay is based on GEANT4 [57] and has been validated with comparisons to data [45].

In comparing the IBD rates among the far hall and near halls, efficiencies and uncertainties common to all the ADs are irrelevant. The AD-uncorrelated uncertainties of the efficiencies, which reflect the identicalness of the ADs, were determined by comparing data among all eight ADs. The uncertainties of ε_μ and ε_m were negligible (see Section IV.2). The remaining quantities in Eq. (12) and their uncertainties, are discussed in this Section. The contribution from IBDs in the MO is described in Section VII.5.

VII.1. Prompt-Energy Selection

The first selection criterion applied to AD events (after rejecting PMT flashes) was $E_{\text{rec}} > 1.5$ MeV. Ultimately, this selection affected only prompt events because of the more stringent requirement applied to delayed events. The prompt-energy selection efficiency and its uncertainty were determined with simulation in which the energy scale was aligned to that of the data (see Section IV.1). The efficiency was defined as the number of IBD reactions N that satisfied the prompt-energy criterion divided by the total number of IBD reactions:

$$\varepsilon_{E_p} = \frac{N(E_p > 1.5 \text{ MeV})}{N_{\text{IBD}}}. \quad (13)$$

The higher-energy requirement of $E_p < 12$ MeV was estimated to contribute negligibly to the inefficiency and uncertainty, as suggested by Fig. 11. The efficiency in the LS volume was lower than that in the GdLS volume because a larger fraction of the annihilation γ 's deposited energy outside the scintillating volumes. This fraction was largest for IBDs occurring in the acrylic elements. The net efficiency of all volumes was about 90%.

The AD-uncorrelated uncertainty of the efficiency was estimated as the change in efficiency after shifting the energy scale by 0.5%. The relative change in efficiency was about 0.1%. The 0.5% shift is an estimate of the AD-uncorrelated uncertainty of the energy scale that was determined by comparing the fitted means of the $n\text{H-IBD}$ γ and ^{212}Bi α peaks of all eight ADs. For reference, the estimated uncertainty of the energy scale in the GdLS volume was 0.2% [12].

VII.1.1. Variation with Baseline

The L/E -dependence of neutrino oscillation [see Eq. (3)] implies that the shape of the neutrino energy spectrum changes with baseline L . Therefore, the efficiency of the prompt-energy criterion varies with baseline. The impact of this dependence on the multiple reactor-detector pairs at Daya Bay was estimated by applying oscillation to a predicted reactor antineutrino spectrum as a function of baseline. At each baseline [36], the IBD selection efficiency was determined with simulation samples for the GdLS, LS, and acrylic volumes. The simulation accounted for energy deposited outside the scintillator volumes, and the nonlinearity [12], nonuniformity, and resolution of the detector energy-response. The oscillation parameter values were the same as those in Section III. The resulting variation in the IBD selection efficiency as a function of baseline is illustrated for the LS region in Fig. 12. The shape of the curve is due to the span of the data in the L/E domain. For the near halls (smaller L), more oscillation occurred for lower energy antineutrinos, which decreased the number of IBD reactions with prompt energy below threshold and thus, increased the efficiency. For illustration, the

mean energy of a prompt event without oscillation was 3.626 MeV while the corresponding energy in EH1 (EH2) due to antineutrinos from the two (four) nearby reactors with oscillation was 3.630 (3.632) MeV. These numbers are representative of the first 4 (8) points in Fig. 12. For the far hall (larger L), more oscillation occurred at median antineutrino energies and about equally at higher and lower energies, resulting in a net decrease in efficiency.

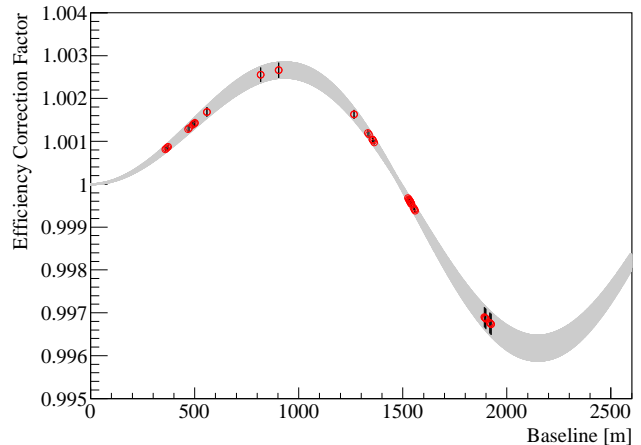


FIG. 12. An example of the relative variation of the IBD selection efficiency with baseline using the value of $\sin^2 2\theta_{13}$ presented in this article. This correction curve is for the LS region. The red circles denote the 48 reactor-detector pairs. Their error bars and the error band are identically defined by the uncertainty of $\sin^2 2\theta_{13}$.

In the fit for $\sin^2 2\theta_{13}$ (Section VIII.2), the IBD selection efficiencies in the GdLS, LS, and acrylic volumes of each AD were multiplied by a correction factor for each reactor baseline (6 reactors \times 8 ADs = 48 baselines) [36]. The fit was first performed without correction factors. The resulting value of $\sin^2 2\theta_{13}$ was then used to generate a set of correction factors and then fit again. This iterative approach was tested using Asimov data samples generated according to Eq. (1) with known values of $\sin^2 2\theta_{13}$. Several values of $\sin^2 2\theta_{13}$ were tested and all fits converged consistently with negligible bias. No additional uncertainty was assigned. Although several iterations were performed, the value of $\sin^2 2\theta_{13}$ converged within the precision reported in this article after only one iteration. The results of the fits without corrections were about 4% larger than the true values for the Asimov data samples and the converged value for the measured data. This variation of the IBD selection efficiency was estimated to be an order of magnitude smaller for the $n\text{Gd-IBD}$ analysis, which required $E_p > 0.7$ MeV.

VII.2. Coincidence-Time Selection

The efficiency of the coincidence-time selection was different for each detector volume v due to the different den-

sities and neutron-capture cross-sections of the materials. The efficiency was defined as

$$\varepsilon_T = \frac{N(1 < t_c < 400 \mu\text{s}; E_p > 1.5 \text{ MeV})}{N(E_p > 1.5 \text{ MeV})}, \quad (14)$$

and was determined with simulation. The efficiency in the LS volume was about 85% and that in the GdLS volume was about 99% due to the shorter neutron-capture time of $n\text{Gd}$. These values were validated with data.

The neutron-capture time was studied in the GdLS and LS volumes by fitting for the mean neutron-capture time with the following formulas:

$$\begin{aligned} N_{\text{Gd}}(t) &= N_{0,\text{Gd}} \cdot \left[(1 + \alpha) \frac{1}{\tau_{\text{Gd}}} e^{-t/\tau_{\text{Gd}}} - \alpha \frac{1}{\tau_0} e^{-t/\tau_0} \right] + C_1 \\ N_{\text{LS}}(t) &= N_{0,\text{LS}} \cdot \frac{1}{\tau_{\text{LS}}} e^{-t/\tau_{\text{LS}}} + C_2, \end{aligned} \quad (15)$$

where α balances two terms, the first corresponding to the capture of a neutron at thermal energies [$O(0.025)$ eV] with time constant τ_{Gd} , and the second representing the difference in capture cross-section between thermal and IBD neutron energies [$O(0.015)$ MeV], with effective time constant τ_0 . The capture-time spectrum in LS is due almost solely to $n\text{H}$ which can be represented by a single exponential. This is because the number of captures per volume per time, which is proportional to the product of capture cross-section and neutron velocity, is essentially independent of energy below IBD neutron energies. For $n\text{Gd}$, this product is much larger at thermal energies than at IBD energies (see, *e.g.* Ref. [58]), effectively yielding two distinct time constants with $\tau_0 < \tau_{\text{Gd}}$. The capture-time constant in LS is denoted by τ_{LS} , and C_1 and C_2 account for accidentals.

The neutron-capture times for the GdLS and LS regions were studied using $n\text{Gd}$ - and $n\text{H}$ -IBDs, respectively. The selection criteria were slightly modified from the nominal IBD criteria: the $n\text{Gd}$ delayed events were selected between 6 and 10 MeV, while the $n\text{H}$ prompt-energy lower limit was increased to 3.5 MeV to minimize the accidental background, and the $n\text{H}$ delayed-energy criterion was fixed to 1.8-2.8 MeV. When fitting the $n\text{Gd}$ -IBD spectrum, the reconstructed positions of the prompt events were required to satisfy $|z| < 1$ m and $r < 1$ m to minimize the fraction of neutrons that originated from, or had any interactions, outside GdLS. Similarly, when fitting the $n\text{H}$ -IBD spectrum, a constraint of $r > 1.7$ m was applied to minimize the fraction of neutrons that originated from GdLS. The fit results using the data from all ADs are shown in Figs. 13 and 14. Good agreement in the slopes is observed between the data and simulation. The fitted capture-time constants were about 28.1 and 216 μs for the GdLS and LS volumes, respectively. For reference, Fig. 6 shows the total capture-time spectra of the far- and near-hall ADs for the nominal $n\text{H}$ -IBD selection criteria before and after subtracting the accidental background.

The AD-uncorrelated uncertainty of the 400 μs criterion in the combined GdLS and LS volume was partly

estimated using β - α events from the ^{214}Bi - ^{214}Po - ^{210}Pb decay chain. These events provided greater statistics than $n\text{H}$ events and were used to determine the variation of the time measurements of the electronics. The lifetime of ^{214}Po is 237 μs , which is close to the mean $n\text{H}$ capture time in LS. The efficiency of the selection was determined relative to the number of double coincidences with a coincidence time window of [1, 1500] μs . The relative differences of the efficiencies of all eight ADs are shown in Fig. 15, and are within 0.1% at the selection criterion of 400 μs .

Similarly, the uncertainty associated with the 1 μs criterion was determined to be 0.1% by comparing the rel-

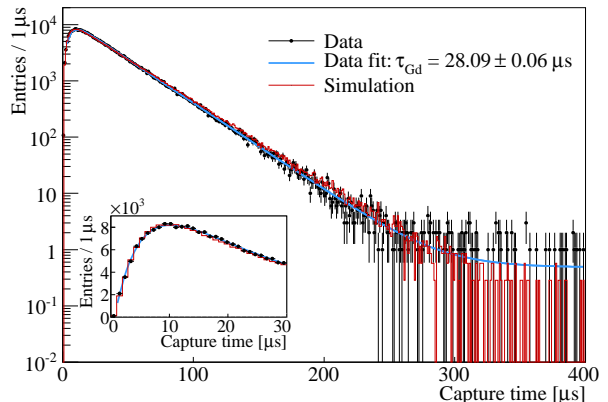


FIG. 13. Time separation for double coincidences selected with $n\text{Gd}$ -IBD criteria in the GdLS volume from the data of all ADs (black points) and from simulation (red histogram). The spectra are normalized by the number of coincidences between 6 and 150 μs . The fit to data (blue curve) and fitted capture-time constant τ_{Gd} are shown.

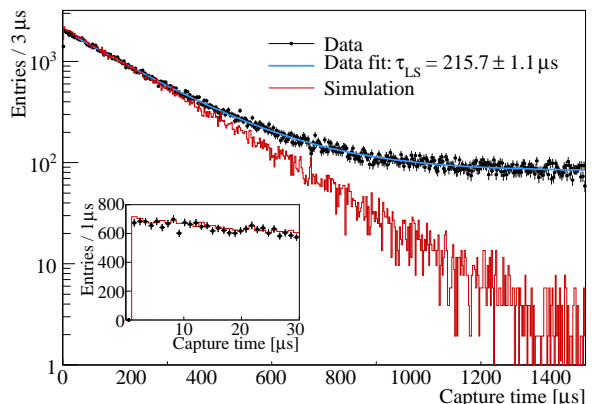


FIG. 14. Time separation for double coincidences selected with $n\text{H}$ -IBD criteria in the LS volume from the data of all ADs (black points) and from simulation (red histogram). The spectra are normalized by the number of coincidences between 30 and 300 μs . The fit to data (blue curve) and fitted capture-time constant τ_{LS} are shown.

ative number of events between 1 and 2 μs .

Because the estimates of the uncertainties were performed using a source different from neutrons, additional uncertainties related to neutron-capture time were added. The uncertainties considered were identified from an expression of the mean neutron-capture time:

$$\frac{1}{\tau} = \frac{v_n}{\lambda} = v_n \sum_i n_i \sigma_i(v_n), \quad (16)$$

where v_n is the velocity of the neutron, λ is the mean free-path of the neutron, n_i is the number-density of nucleus i , and σ_i is the neutron-nucleus cross-section. Isotopes other than Gd and H contributed less than 1% of captures and were not considered. For the LS volume, the measured density differed by $< 0.1\%$ among the ADs. In addition, the fluctuation in density caused by temperature changes uncorrelated among experimental halls was within 0.045% during the data-recording period. These effects introduced a $< 0.11\%$ uncertainty to the neutron-capture time τ . This uncertainty was propagated through Eq. (15) to obtain an approximate 0.02% AD-uncorrelated uncertainty.

The uncertainties from the ^{214}Bi β - α event comparisons and neutron-capture time-related quantities were combined to give a total AD-uncorrelated uncertainty of 0.14% for the efficiency of the coincidence-time criterion.

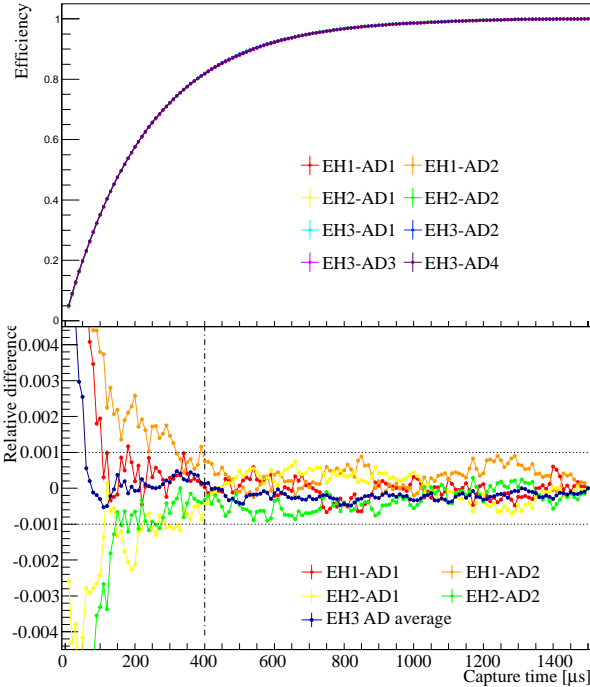


FIG. 15. Efficiency (top panel) and relative difference to the average (bottom panel) *vs.* event time separation for ^{214}Bi β - α events in each AD. The data of the far-hall ADs were combined in the bottom panel to increase statistics. The differences are within $\pm 0.1\%$ at the criterion of 400 μs .

VII.3. Delayed-Energy Selection

The efficiency of the delayed-energy selection was determined with simulation and defined as

$$\varepsilon_{E_d} = \frac{N(E_d \pm 3\sigma; 1 < t_c < 400 \mu\text{s}; E_p > 1.5 \text{ MeV})}{N(1 < t_c < 400 \mu\text{s}; E_p > 1.5 \text{ MeV})}. \quad (17)$$

This definition does not preclude IBDs with the neutron captured by nuclei other than hydrogen; for example, $n\text{Gd}$ IBDs comprised approximately 0.7% of the IBDs after applying the delayed-energy criterion. For both simulation and data, the $\mu \pm 3\sigma$ selection was applied using the mean μ and standard deviation σ from a fit of the delayed-energy spectrum with the Crystal Ball function [46]. The selection efficiency in the GdLS volume was about 15% primarily because of neutron-capture by gadolinium. The efficiency in the LS volume was about 65% primarily because of the outward escape of the $n\text{H}$ γ 's.

Two methods were used to estimate the AD-uncorrelated uncertainty of the delayed-energy selection efficiency. One method is a relative comparison of the delayed-energy spectra of the ADs. The comparison was made after applying all the $n\text{H}$ selection criteria and subtracting the accidental backgrounds (errors from accidental subtractions were included in the energy spectra). The method uses the number of events within two energy ranges: the first is the nominal selection of $\mu \pm 3\sigma$, which is approximately [1.90, 2.74] MeV, and the second is [1.50, 2.80] MeV. These two ranges are visible for each AD in Fig. 16. The upper value of the latter range was chosen to include most of the $n\text{H}$ IBDs with $E_d > 2.74$ MeV (0.1% of $n\text{H}$ IBDs) while the lower value corresponds to the low-energy criterion (Section IV.2.2) and includes more of the tail of the spectrum (12% more $n\text{H}$ IBDs). The latter range contains both peak and tail portions of the spectrum and therefore is assumed to be sensitive to all factors that might influence the shape of the spectrum.

For each AD i , the number of events in the nominal range A ($N_{A,i}$) was plotted *vs.* the number of events in the extended range B ($N_{B,i}$) and a linear relation was fit:

$$\overline{N}_A(N_{B,i}) = a + bN_{B,i}. \quad (18)$$

This line represents the average behavior of all ADs, including differences in their spectral shape and backgrounds. Here, the efficiency of the delayed-energy selection ε is defined as N_A/N_{Total} , where N_{Total} is the number of events without the delayed-energy selection. The fitted line was used to determine the relative variation of ε for each AD:

$$\frac{\delta\varepsilon_i}{\varepsilon_i} = \frac{\delta N_{A,i}}{N_{A,i}} = \frac{N_{A,i} - \overline{N}_A}{N_{A,i}} = 1 - \frac{a + bN_{B,i}}{N_{A,i}}. \quad (19)$$

This determination assumes that there is no variation in N_{Total} . From studies with simulation, it was found that

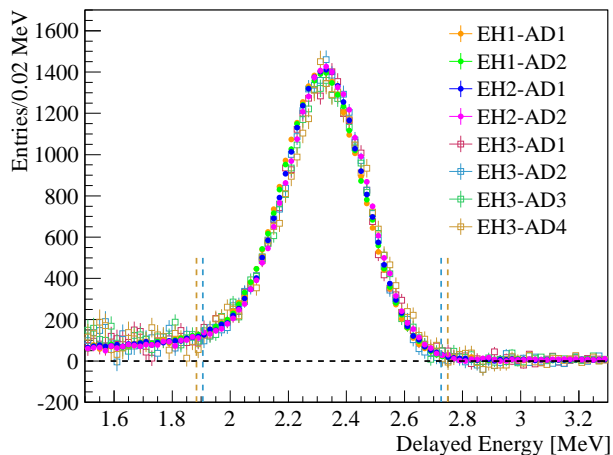


FIG. 16. Delayed energy spectra of $n\text{H}$ -IBDs in all ADs. The entries of each histogram are normalized to the average number of IBDs in the far-hall ADs. The fitted means are scaled to the average of the mean of the far-hall ADs. The two pairs of vertical lines correspond to the largest and smallest 3σ selections.

N_A and N_{Total} are highly correlated under various scenarios that could modify the shape of the spectrum, including differences in OAV dimensions [35] and the residual nonuniformity of E_{rec} , making this assumption conservative. This determination also assumes that variations in the spectrum outside range B are not systematically different from those within. Using simulation, differences in OAV dimensions or in the mean free path of the γ 's were found to have a greater impact on the shape of the spectrum at the low-energy end, but to contribute negligibly to $\delta\varepsilon_i/\varepsilon_i$. In addition, comparing the high-statistics spectra of the near-hall ADs did not reveal any systematic trends in the differences among spectra above 1.5 MeV, suggesting that there may not be any such trends below 1.5 MeV. The statistical uncertainties of the data from the far-hall ADs were large, so they were excluded from the determination though they were conservatively used in the linear fit. Comparing the four near-hall ADs, the half-range of the $\delta\varepsilon_i/\varepsilon_i$ was 0.33%. This estimation directly includes AD-to-AD variations in the 3σ selection, energy scale, and factors that may influence the shape of the spectrum; however, it does not include variations in the fraction of neutrons that capture on hydrogen (53%) relative to other isotopes, such as Gd (46%) and C (0.5%), because such variations have an equivalent impact on N_B and N_A .

The fraction of neutrons that capture on isotope x is expressed similarly as the mean capture time in Eq. (16):

$$f_x = \frac{n_x \sigma_x(v_n)}{\sum_i n_i \sigma_i(v_n)}. \quad (20)$$

Performing error propagation on Eq. (16) and Eq. (20), and combining the results, the variation of f_x among the ADs was expressed in terms of the variation of τ and

one of the n_i . In this way, the variation of the measured capture time in the GdLS was used to constrain the variation of n_{Gd} . The variation of n_{H} was taken to be negligible because of the mixing of all production batches of scintillator [32] and the filling procedures applied to the ADs [59]. As a result, the AD-to-AD variation of the fraction of $n\text{H}$ captures was estimated to be $< 0.01\%$ and 0.16% in the LS and GdLS volumes, respectively. These two values correspond to approximately 0.03% for the full volume.

Combining the variations estimated from the spectral comparison and the $n\text{H}$ capture-fraction calculation yields a total AD-uncorrelated uncertainty of 0.33% for the delayed-energy selection efficiency.

The second method used to evaluate the uncertainty of the delayed-energy selection efficiency is the ratio of the numbers of spallation $n\text{H}$ to spallation $n\text{Gd}$ ($N_{n\text{H}}/N_{n\text{Gd}}$), which utilizes the smaller variation of the $n\text{Gd}$ delayed-energy selection efficiency and the larger sample of spallation neutrons. The energy spectrum of spallation- $n\text{H}$ and $n\text{Gd}$ γ 's from each AD was obtained by subtracting a background spectrum recorded in a background time window from the spectrum recorded in a signal time window. Spallation neutrons generated by cosmogenic muons were identified as delayed-type events that followed WS- or AD-identified muons. These muons were identified with greater purity by augmenting the definitions of a μ_{WS} and μ_{AD} : for both the IWS and OWS, N_{PMT} was required to be > 20 , and a μ_{AD} was required to have $E_{\text{rec}} > 50$ MeV. A $20\text{-}\mu\text{s}$ muon-event veto-time was applied to avoid the “ringing” of PMT signals that followed high-energy events [60]. The signal time window was between 20 and $700\ \mu\text{s}$ after a muon event. The background time window was a similar length, however, given the different distributions of muon energy and trajectory among halls [30] (which affected the characteristics of the spallation products), the background window was tuned to be slightly different in each hall. By matching both the shape and population of the tail portions of the signal and background energy spectra, the background window was set to be between 700 and 1480, 1453, and $1384\ \mu\text{s}$, in EH1, EH2, and EH3, respectively. Both $n\text{Gd}$ and $n\text{H}$ delayed-energy criteria were nominal (see Table 1).

The energy spectra of the spallation-neutron-capture γ 's were fitted with signal and background components. The background component accounted for residual spallation products that were not subtracted with the background window. For the $n\text{H}$ spectrum, the signal component was a Crystal Ball function and the background function was a second-order polynomial. For $n\text{Gd}$, the signal component was two Crystal Ball functions as mentioned in Section IV.1, and the background function was a first-order polynomial. Fit results are shown in Figs. 17 and 18, where the number of signal events defined as spallation neutrons are labeled as “Nsig”.

Compared with the previous analysis [15], the spallation neutron ratio is updated in this article by normalizing the number of neutrons to the number of target

protons N_p (Section VII.6):

$$\frac{N_{nH}/(N_{p,LS} + r_\varepsilon N_{p,GdLS})}{N_{nGd}/N_{p,GdLS}}, \quad (21)$$

where r_ε is the ratio of efficiencies of selecting spallation nH in GdLS *vs.* LS: $r_\varepsilon \equiv \varepsilon_{GdLS}/\varepsilon_{LS}$. Due to the non-uniform distribution of spallation neutrons, r_ε is not precisely known; therefore, two extreme cases were considered: a) the distribution is entirely within the LS ($r_\varepsilon = 0$); b) the distribution is uniform ($r_\varepsilon = 0.22$ from simulated IBDs). Figure 19 shows the difference in the ratio defined by Eq. (21) for each near-hall AD relative to the mean of the four ADs. The far-hall ADs were not used due to their lack of statistics. The choice of r_ε is found to have little impact on the variation of the ratio.

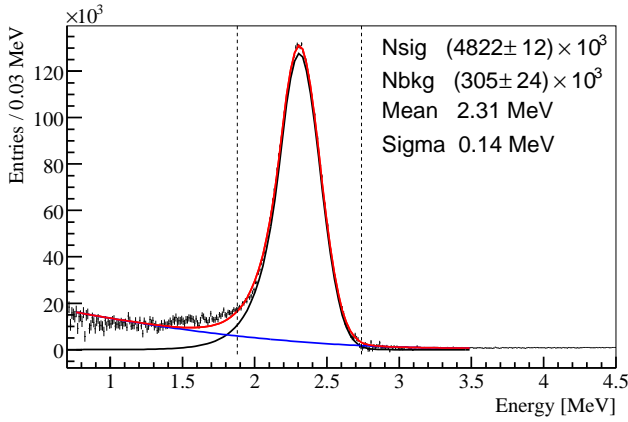


FIG. 17. Fit of the spallation- nH reconstructed energy spectrum (black points) with a Crystal Ball function (black line) and a second-order polynomial (blue line) in EHI-AD1. The red line is the sum of the black and blue lines. The vertical dashed lines represent the delayed-energy selection criteria (Mean \pm 3Sigma) within which Nsig and Nbkg were counted.

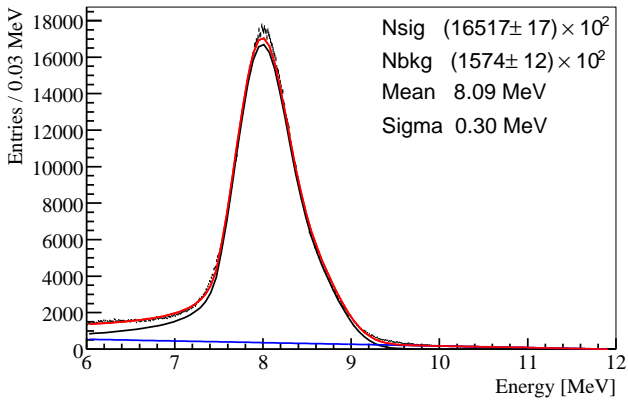


FIG. 18. Fit of the spallation- nGd reconstructed energy spectrum (black points) with two Crystal Ball functions (black line) and a first-order polynomial (blue line) in EHI-AD1. The red line is the sum of the black and blue lines.

The half-range of the ratios of the near-hall ADs is approximately 0.35%. Due to the use of a ratio with nGd events, this estimation inherently includes the variation of the nGd delayed-energy criterion, which was estimated to be 0.12% for IBDs [50]. This estimate also inherently includes the variation of the fraction of neutrons that capture on hydrogen.

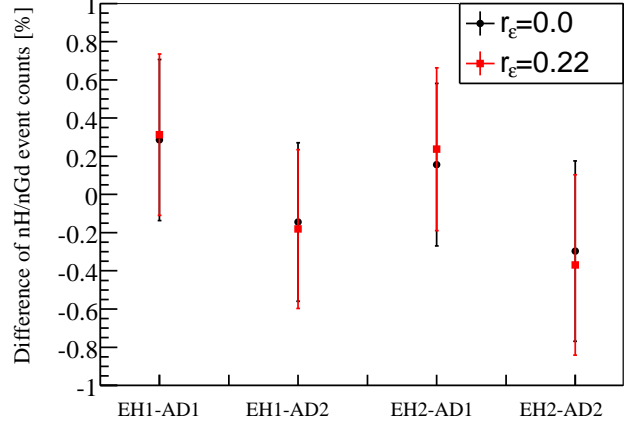


FIG. 19. Difference in the ratio of the number of spallation- nH / $-nGd$ events in the fitted energy peaks of each near-hall AD relative to the mean of all near-hall ADs. See the text for details.

Given the 0.33% and 0.35% relative uncertainties from the two independent methods, 0.35% was assigned for the total AD-uncorrelated uncertainty of the delayed-energy selection efficiency.

To determine the correlation of the delayed-energy selection efficiency between the nH and nGd analyses, the uncertainty was decomposed into three components: 3σ variation, energy scale variation, and others. The contributions of the first two components were estimated with simulation by applying the largest and smallest 3σ ranges (see Fig. 16) and shifting the energy scale (see Section VII.1), respectively. The first component, which was dominant, does not exist for the nGd -IBD analysis and thus, is uncorrelated. The correlation of energy scale variations between the nH - and nGd -IBD analyses was estimated to be 0.8 with a linear fit of the measured nH -IBD *vs.* nGd -IBD delayed-energy peaks. The latter component of “others” accounts for any contributions not directly evaluated, such as differences in OAV dimensions or the residual nonuniformity of E_{rec} , and was assumed to be fully correlated. The hydrogen capture fractions of the nH analysis were determined to be anticorrelated with the gadolinium capture fraction of the nGd analysis: in the GdLS volume, if the fraction of captures on Gd increases, then naturally the fraction on H decreases. In the LS volume, the same anticorrelated relation exists via neutrons that are produced in GdLS or LS but capture in the other of the two volumes. Combining the correlation constants and corresponding component uncertainties from both the nH and nGd analyses yields an

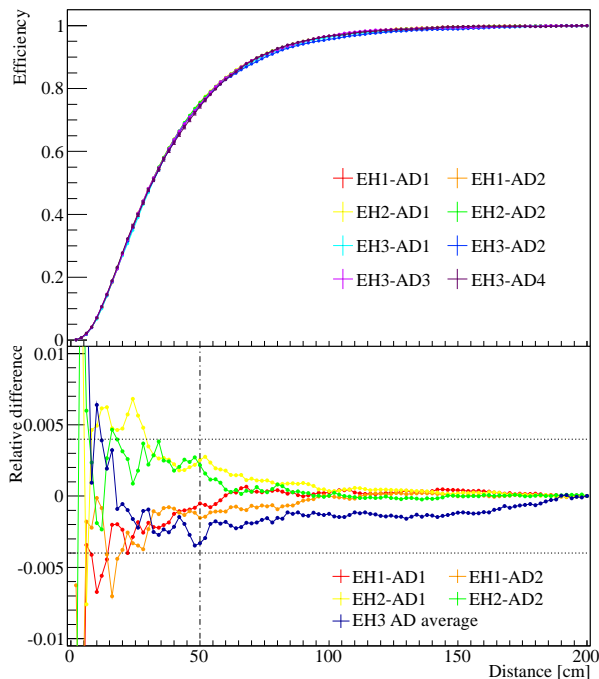


FIG. 20. Efficiency (top panel) and relative difference to the average (bottom panel) *vs.* coincidence-distance for correlated double coincidences (N_{Cor}) in each AD. The data of the far-hall ADs were combined to increase statistics. The differences are within $\pm 0.4\%$ at the criterion of 50 cm.

overall correlation coefficient of 0.07 for the efficiency of the delayed-energy selection.

VII.4. Coincidence-Distance Selection

The efficiency of the coincidence-distance selection was measured with data and defined as

$$\varepsilon_D = \frac{N(d_c < 50 \text{ cm}; E_d \pm 3\sigma; \dots; E_p > 1.5 \text{ MeV})}{N(E_d \pm 3\sigma; 1 < t_c < 400 \mu\text{s}; E_p > 1.5 \text{ MeV})}. \quad (22)$$

The efficiency was determined relative to the number of DCs with $d_c < 200$ cm using the data of all 8 ADs with accidental backgrounds subtracted as shown in Fig. 5. The efficiency curves and relative differences with respect to the average are shown in Fig. 20. The efficiency for $d_c < 50$ cm was about 75%. Because the total statistics of the far-hall ADs was only about half that of a single near-hall AD, the data of the four far-hall ADs were merged together when calculating the relative difference. All the differences were within $\pm 0.4\%$ at the 50-cm selection criterion. Therefore, the AD-uncorrelated uncertainty of the efficiency of the coincidence-distance criterion was assigned to be 0.4%.

VII.5. IBDs in Acrylic and Mineral Oil

The target materials were primarily liquid scintillator, however, the IAV, OAV, and acrylic-encased reflectors were in direct contact or close proximity with the scintillators such that an IBD positron originating in these elements could enter the scintillators and deposit sufficient energy to trigger an AD. Such IBDs contributed an estimated 1.0% of the $n\text{H}$ -IBDs after selection.

IBD positrons originating in the MO rarely reached the scintillator and generally produced an insufficient amount of light to trigger an AD. However, a few percent of the IBD positrons annihilated in-flight, producing a higher-energy γ that was sometimes directed toward the scintillator with enough energy to pass the low-energy criterion. Some fraction of the corresponding IBD neutrons propagated to the LS and captured on H. From simulation, it was estimated that approximately 0.06% of the IBDs in the MO survived the selection criteria. This “spill-in” effect from the MO was found to have a negligible impact on the determination of $\sin^2 2\theta_{13}$ and was not included in this analysis.

The impact of neutrons or γ 's (and their secondaries) that spill-out into the MO, or spill-in/out between the GdLS and LS, is naturally included in the prompt- and delayed-energy selection efficiencies and their uncertainties.

VII.6. Target Proton Number

The number of target protons N_p was determined for each AD from the measured target masses M and hydrogen mass-fractions w_{H} of the GdLS, LS, and acrylic volumes v :

$$N_{p,v} = M_v w_{\text{H},v} N_{\text{A}} / m_{\text{H}}, \quad (23)$$

where N_{A} is Avogadro's number and m_{H} is the molar mass of hydrogen.

The mass-fractions of hydrogen were determined by combustion analysis to be about 12.0% for both GdLS and LS (with uncertainties at the level of 0.1%) [35]. For acrylic ($\text{C}_5\text{H}_8\text{O}_2$), $w_{\text{H}} = 8.05\%$. The AD-uncorrelated uncertainties of these quantities were taken to be negligible as described for n_{H} in Section VII.3.

The total masses of GdLS and LS were measured when filling each AD, using a load cell and Coriolis flow meter, respectively [59]. The masses of acrylic components were measured with an industrial scale before filling [31]. The relevant masses are given for each AD [36]. Only the uncertainties of target mass were propagated to the final uncertainty of target proton number.

The average numbers of target protons in the GdLS, LS, and acrylic volumes are 1.43×10^{30} , 1.54×10^{30} , and 0.18×10^{30} , respectively. Values for each AD are provided [36]. The AD-uncorrelated uncertainties are listed in Table III.

VII.7. Detector Leak

Around the end of July, 2012, when data-recording was paused to install the final two ADs, a leak began between the LS and MO volumes of EH3-AD1. The levels of GdLS and LS in the overflow tanks [61] (see Fig. 1) of EH3-AD1 slowly decreased while the level of MO slowly increased, suggesting that the LS was leaking into the MO region. This hypothesis was supported by measurements using the MO clarity system [35] which showed significant decreases in the transmission of shorter-wavelength light through the MO and an increase of MO light yield over time, consistent with a gradual addition of scintillator into the MO. The hypothesis was further supported by the observation of an increased (decreased) rate of higher-energy (lower-energy) muons reconstructed in the MO volume. These observed trends stabilized after about two years with an estimated leakage of about 20 kg. This loss of mass lowered the height of the LS level in the overflow tank and did not directly impact the number of target protons in the LS volume.

No impact on the detector response is expected in the LS volume due to the direction of the leak; however, in the MO volume, there is potential for an increase in trigger rate. Given a 20-kg leakage into the 36-ton volume, and assuming the light yield of the LS is two orders of magnitude greater than that of the MO, one may naively estimate an average increase of the light yield in the MO volume on the order of 1%. In simulation, this increase was modeled as an increase in the energy scale, and was applied to prompt and delayed events of IBDs generated in the MO, resulting in a $O(0.001)\%$ increase of the $n\text{H}$ -IBD selection efficiency. Indeed, no impact of the leak to the $n\text{H}$ -IBD analysis has been observed in comparisons of various quantities before and after the start of the leak. These quantities included various event rates, neutron-capture energy peak and resolution, and IBD prompt and delayed event-position distributions. Given the observed stabilization of the leak, no impact is expected in the future.

VII.8. Summary

The efficiencies of the PMT flash rejection, prompt- and delayed-energy selection, and coincidence-time selection criteria were determined with simulation, while the number of target protons, the muon-veto and multiplicity and coincidence-distance selection efficiencies were determined with data. The AD-uncorrelated uncertainties of these quantities were determined by comparing data among the eight ADs.

The efficiency of the PMT flash rejection criterion was $> 99.99\%$ (see Section IV.2.1) and had a negligible uncertainty. Muon-veto and multiplicity selection efficiencies (ε_μ and ε_m) are listed in Table II and had negligible AD-uncorrelated uncertainties. The product of the efficiencies of the prompt- and delayed-energy, and time

selection criteria were about 14%, 50%, and 5% in the GdLS, LS, and acrylic volumes, respectively. The efficiency of the coincidence-distance criterion was determined as an average for all volumes: 75%. The AD-uncorrelated uncertainties of these efficiencies are listed for each detector volume v in Table III. The uncertainty of the delayed-energy selection efficiency reduced from 0.5% [15] to 0.35% because of a new estimation and an update of the original estimation to scale the number of spallation neutrons with the number of target protons. This reduced the uncertainty of the $n\text{H}$ -IBD selection efficiency by 15%.

	Uncertainty (%)	Correlation
Target protons ($N_{p,\text{GdLS}}$)	0.03	1
Target protons ($N_{p,\text{LS}}$)	0.13	0
Target protons ($N_{p,\text{acrylic}}$)	0.50	-
Prompt energy (ε_{E_p})	0.10	1
Coincidence time (ε_T)	0.14	1
Delayed energy (ε_{E_d})	0.35	0.07
Coincidence distance (ε_D)	0.40	0
Combined (N_ε)	0.57	0.07

TABLE III. The relative per-detector uncorrelated uncertainties for each detector-related quantity. The uncertainties of the N_p are weighted when determining the combined uncertainty of N_ε in the bottom row. The last column contains the estimated correlation coefficients between the $n\text{H}$ - and $n\text{Gd}$ -IBD analyses.

Table III also gives the estimated correlation coefficients between the detector efficiencies of the $n\text{H}$ - and $n\text{Gd}$ -IBD analyses. The number of target protons were fully correlated in the GdLS while uncorrelated in the LS due to their identical and independent methods of mass measurement, respectively. The efficiency of the prompt-energy criterion was correlated through a common dependence on energy scale, and was conservatively treated as fully correlated. The coincidence-time criterion was also treated as fully correlated. The delayed-energy criterion was largely independent because the primary contribution to the uncertainty in the $n\text{H}$ analysis was the variation of the 3σ selection, which does not exist in the $n\text{Gd}$ analysis. The coincidence-distance criterion was uncorrelated because there was no such selection in the $n\text{Gd}$ -IBD analysis. The overall correlation between the IBD detection efficiencies of the $n\text{H}$ - and $n\text{Gd}$ -IBD analyses was about 0.07.

The last row of Table II shows the ratio of the efficiency- and target proton-corrected rates of IBDs for the $n\text{H}$ - and $n\text{Gd}$ -IBD analyses, for each AD. The errors are the statistical, background, and AD-uncorrelated systematic uncertainties of both analyses. The consistency of the eight values with one another reflects the consistency of the selected number of IBDs, background estimates, and per-AD target proton and efficiency corrections, between the two analyses. The consistency of the eight values with 1 reflects the accuracy of these values for both analyses.

VIII. RESULTS

The measured and predicted IBD rates of each hall are shown over time in Fig. 21. The measured rates are background-subtracted and efficiency-corrected ($\varepsilon_\mu\varepsilon_m$). The predictions are from Eq. (1) [*i.e.*, Eqs. (2) and (12)], and are adjusted with the best-fit normalization factor ϵ from Eq. (28). The six reactors are seen to have operated continually at their nominal power output. The two reactors nearby EH1 were refueled every 16 months and the four reactors nearby EH2 were refueled every 8-12 months, each with 1-2 months downtime.

VIII.1. Antineutrino Disappearance

The disappearance of $\bar{\nu}_e$ is quantified without invoking a model of neutrino oscillation and with minimal impact from models of reactor antineutrino spectra, by directly comparing the measured IBD rate at the far hall with the rate expected based on the measurements at the near halls. The expected number of IBDs in the far hall was expressed as a combination of the two near-hall measurements:

$$\bar{N}_{\text{EH3}} \equiv \alpha N_{\text{EH1}} + \beta N_{\text{EH2}}, \quad (24)$$

where N_{EH1} and N_{EH2} are the measured numbers of IBDs after subtracting all the backgrounds and correcting for

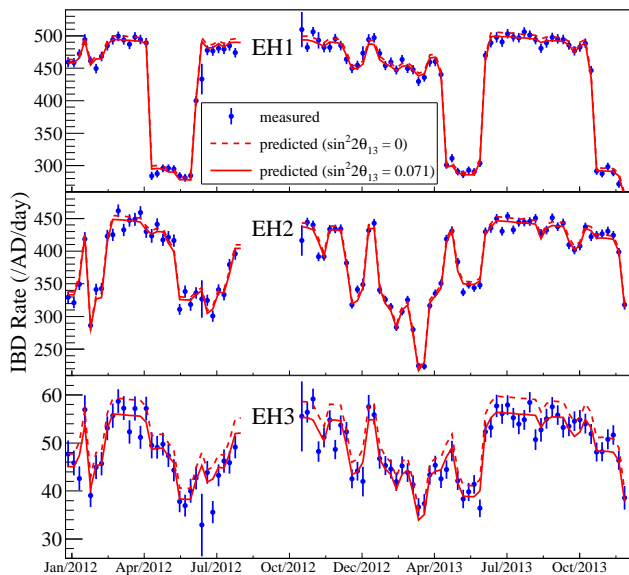


FIG. 21. Measured IBD rate *vs.* time for each experimental hall (blue points). Each point spans one week and the error bars are purely statistical. The dashed red lines are the expected IBD rates assuming no oscillation. The solid red lines are the expected IBD rates with the best-fit value of $\sin^2 2\theta_{13}$. The final two of eight ADs were installed during the ≈ 12 -week gap in all halls.

the muon-veto and multiplicity selection efficiencies (ε_μ and ε_m) in EH1 and EH2.

Expressions for the weights α and β were determined using Eq. (24) with the number of measured IBDs replaced by the number of predicted IBDs assuming no oscillation. This number was calculated for experimental hall i using Eq. (1) without oscillation:

$$\bar{N}_i = \sum_{r=1}^6 \bar{N}_{ir} \equiv \sum_{r=1}^6 \sum_{d_i} \frac{N_{\varepsilon, d_i}}{4\pi L_{d_i}^2} \iint_{\{t_{d_i}\}} \sigma_\nu \frac{d^2 N_r}{dE dt} dE dt, \quad (25)$$

where d_i denotes the d -th AD in experimental hall i and the N_ε do not include ε_m and ε_μ . The modified Eq. (24) directly yields $\beta = (\bar{N}_3 - \alpha\bar{N}_1)/\bar{N}_2$. The weight α was obtained by operating on the difference between the two predictions for EH3: $\Delta\bar{N} = \bar{N}_3 - \alpha\bar{N}_1 - \beta\bar{N}_2$. The variance of $\Delta\bar{N}$ (σ_Δ^2) was obtained via error propagation with respect to the reactor-uncorrelated relative uncertainty (which was taken to be identical for all reactors), and then its minimum was found with respect to α , yielding

$$\alpha = \frac{\sum_r (\bar{N}_{3r} - \frac{\bar{N}_3}{N_2} \bar{N}_{2r}) (\bar{N}_{1r} - \frac{\bar{N}_1}{N_2} \bar{N}_{2r})}{\sum_r (\bar{N}_{1r} - \frac{\bar{N}_1}{N_2} \bar{N}_{2r})^2}. \quad (26)$$

This expression minimizes the impact of the reactor-uncorrelated uncertainty.

For the 621-day data set used in this analysis, $\alpha = 0.054$ and $\beta = 0.216$. These values are dominated by the baselines L_{dr} , and only slightly influenced by the integrated emission rates $d^2 N_r(E, t)/dE dt$. Thus, β , which is associated with EH2, is four times larger than α primarily because of the shorter baselines between EH3 and the four reactors nearby EH2. The reactor-uncorrelated uncertainty is suppressed by a factor of about 20, which can be seen by evaluating the expression for σ_Δ^2 .

Using Eq. (24) and the values of α and β , the ratio of the observed to the expected number of IBDs at the far hall was

$$R \equiv \frac{N_{\text{EH3}}}{\bar{N}_{\text{EH3}}} = 0.950 \pm 0.005. \quad (27)$$

Figure 22 shows the measured prompt-energy spectrum at the far hall and that predicted with the near-hall measurements via Eq. (24). The ratios R of each energy bin are shown in the bottom panel and demonstrate the effect of $\bar{\nu}_e$ disappearance as a function of energy. The best-fit curve is the ratio of far-hall and normalized near-hall predictions using Eq. (1) and the result for $\sin^2 2\theta_{13}$ presented in the next section.

VIII.2. Fit for $\sin^2 2\theta_{13}$

To determine $\sin^2 2\theta_{13}$, a χ^2 was constructed with pull terms for the background uncertainties and the AD- and

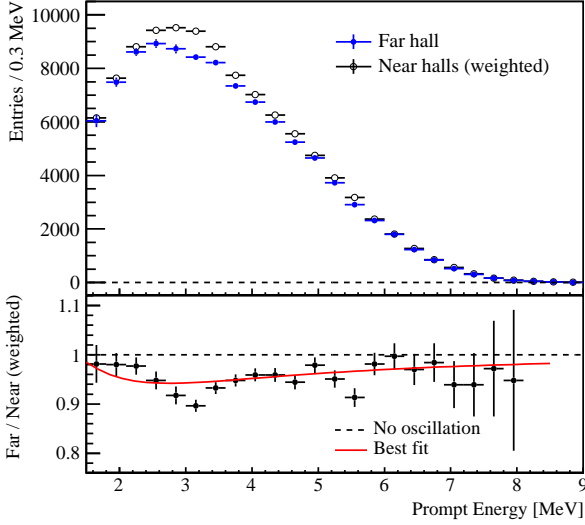


FIG. 22. Top: Reconstructed prompt-energy spectrum of the far hall (solid blue points) and the expectation based on the measurements of the two near halls (empty black points). Spectra are background-subtracted. Error bars are purely statistical. Bottom: Ratio of the Far/Near halls and the curve representing the best-fit value of $\sin^2 2\theta_{13} = 0.071 \pm 0.011$.

reactor-uncorrelated uncertainties:

$$\chi^2 = \sum_{d=1}^8 \frac{[N_{\text{DC},d} - \bar{N}_{\text{IBD},d}(1 + \epsilon + \sum_{r=1}^6 \omega_r^d \alpha_r + \epsilon_d) - (1 + \eta_d)B_d]^2}{(\sigma_{\text{DC},d})^2} + \sum_{r=1}^6 \frac{\alpha_r^2}{\sigma_R^2} + \sum_{d=1}^8 \left(\frac{\epsilon_d^2}{\sigma_D^2} + \frac{\eta_d^2}{(\sigma_{B,d})^2} \right), \quad (28)$$

where $N_{\text{DC},d}$ is the number of measured double coincidences from the d -th AD given in Table II, B_d is the sum of the accidental and correlated backgrounds derivable from Table II, $\sigma_{\text{DC},d}$ is the statistical uncertainty of N_{DC} , and \bar{N}_{IBD} is the expected number of IBDs from Eq. (1), which contains the oscillation parameter $\sin^2 2\theta_{13}$. The ω_r^d [36] are the fractions of IBDs in the d -th AD due to the r -th reactor, which were calculated using Eq. (1) without oscillation (including oscillation decreased the best-fit value of $\sin^2 2\theta_{13}$ by less than 0.03%). The reactor-uncorrelated uncertainty (0.9%) is denoted as σ_R . The parameter σ_D is the AD-uncorrelated uncertainty of IBD detection efficiency from Table III. The parameter $\sigma_{B,d}$ is the combination of all background uncertainties, which are given in Table II. There are twenty two corresponding pull parameters denoted as α_r , ϵ_d , and η_d . The normalization factor ϵ was fit and accounted for any biases in the backgrounds B_d that were common to all halls or detectors, and any biases in the predicted number of IBDs $\bar{N}_{\text{IBD},d}$ that were common to all detectors; *i.e.*, in reactor-related models/quantities, the IBD cross-section model, or IBD selection efficiencies.

Iterating over $\sin^2 2\theta_{13}$ with the efficiency correction

factors as described in Section VII.1.1, the best-fit value for both the normal and inverted neutrino-mass hierarchies was

$$\sin^2 2\theta_{13} = 0.071 \pm 0.011, \quad (29)$$

with a χ_{min}^2 per degree of freedom of 6.3/6.

Figure 23 shows the ratio of the measured rate to the predicted rate assuming no oscillation, for each detector. The most recent $n\text{Gd}$ result from Daya Bay [12] is included for comparison. The 5.0%-deficit of EH3 relative to the near halls given in Eq. (27) is apparent. For the $n\text{Gd}$ -IBD analysis, this deficit was about 5.2%, and the best-fit value was $\sin^2 2\theta_{13} = 0.084$. The red curve is the oscillation survival probability P_ν of Eq. (3) with a value of $\sin^2 2\theta_{13} = 0.082$ from the combination of the $n\text{H}$ - and $n\text{Gd}$ -IBD analyses, which is described in the next section.

The contributions of various quantities to the total uncertainty of $\sin^2 2\theta_{13}$ (σ_{total}) are listed in Table IV, where they are presented as fractions of σ_{total}^2 . The variance of a quantity was estimated as σ_{total}^2 minus the square of the fit error when fixing the nuisance parameter of said quantity to its best-fit value. The sum of the fractions is not equal to 1 due to correlations. The statistical uncertainty is the largest individual component. The second- and third-largest uncertainties are those of the coincidence-distance criterion and the delayed-energy criterion (see

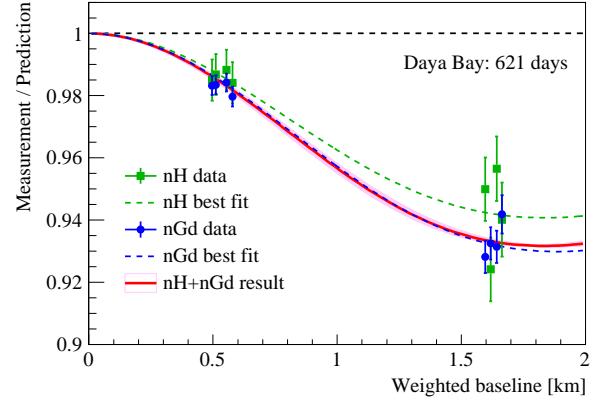


FIG. 23. Ratio of measured to predicted IBD rate in each detector assuming no oscillation *vs.* flux-weighted baseline. Each detector is represented with a green square (blue circle) for the $n\text{H}$ ($n\text{Gd}$) analysis. Error bars include statistical, detector-related, and background uncertainties. The dashed green (blue) curve represents the neutrino oscillation probability using the $n\text{H}$ ($n\text{Gd}$) result for $\sin^2 2\theta_{13}$ and the global fit value of Δm_{32}^2 (the $n\text{Gd}$ result for Δm_{ee}^2 [12]). The solid red curve represents the oscillation probability using the $n\text{H}$ - $n\text{Gd}$ combined result and Δm_{32}^2 , and its magenta error band is from the uncertainty of Δm_{32}^2 . The baselines of EH1-AD2 and EH2-AD2 are shifted by +20 m, and those of EH3-AD1, 2, 3, and 4 are shifted by -30, -10, +10, and +30 m, respectively, for visual clarity.

Table III for the components of the detector contribution). The reactor-uncorrelated uncertainty is reduced by a factor of 20, as in the relative expression of Eq. (27).

	Uncertainty Fraction (%)	Correlation
Statistical	51.8	0
Detector	39.2	0.07
Reactor	4.2	1
${}^9\text{Li}/{}^8\text{He}$	4.4	0
Accidental	0.4	0
Fast neutron	0.3	0
Am-C	0.1	0.7
Combined	100.4	0.02

TABLE IV. Contributions of individual uncertainties to the total uncertainty of $\sin^2 2\theta_{13}$. See the text for details. Detector uncertainties are characterized in Table III. The last column contains the estimated correlation coefficients between the $n\text{H}$ - and $n\text{Gd}$ -IBD analyses.

VIII.3. $n\text{H}$ - $n\text{Gd}$ Combined Result

The result for $\sin^2 2\theta_{13}$ from the current analysis was combined with that from the most recent $n\text{Gd}$ -IBD spectral analysis from Daya Bay [12]. The combination was performed both analytically and via a simultaneous fit of the $n\text{Gd}$ -IBD and $n\text{H}$ -IBD data sets. Correlations between the two analyses were estimated for efficiencies, backgrounds, and reactor-related quantities.

The correlation coefficients of the various uncertainty components are listed in Tables III and IV. Reactor-related uncertainties are fully correlated and statistical uncertainties are uncorrelated. The correlation of quantities with negligible uncertainty, such as DAQ time and muon-veto efficiency, had negligible impact. The correlation coefficients of the detector-related quantities are described in Section VII.8 and listed in Table III. The accidental backgrounds were treated as uncorrelated because of the distinct methods and event samples used in the $n\text{H}$ - and $n\text{Gd}$ -IBD analyses. The Am-C background was estimated to have a correlation coefficient of 0.7, while the other backgrounds were uncorrelated (see Section VI).

The procedure to analytically combine the analyses is the same as that used for the previous combination [15]. Updated values for backgrounds, efficiencies, and the fraction of uncertainty due to statistics were taken from Ref. [12], for the $n\text{Gd}$ -IBD analysis. For the $n\text{H}$ -IBD analysis, these values are listed in Tables II, III, and IV, respectively.

Using the correlation coefficients presented in this article, these values give an overall correlation coefficient of 0.02 between the two analyses, indicating essentially independent determinations of $\sin^2 2\theta_{13}$. Though the correlation will increase as the fraction of statistical uncertainty decreases, this value is smaller than the previous

correlation coefficient of 0.05 [15] primarily because of the distinct estimation of the $n\text{H}$ - ${}^9\text{Li}$ background and the significant reductions in the systematic uncertainties of the Am-C backgrounds for both analyses.

With the $n\text{Gd}$ -IBD result of $\sin^2 2\theta_{13} = 0.084 \pm 0.005$ and the $n\text{H}$ -IBD result of 0.071 ± 0.011 , both the analytical calculation and simultaneous fit resulted in

$$\sin^2 2\theta_{13} = 0.082 \pm 0.004, \quad (30)$$

which is an 8% improvement in precision.

VIII.4. Independent Analysis

The present $n\text{H}$ -IBD analysis was cross-checked with an independent analysis based on a different analysis framework [62]. IBD candidates were independently selected using the same criteria (see Table I) and the backgrounds and muon-veto efficiencies were independently evaluated. Using the χ^2 in Eq. (28), the best-fit value was $\sin^2 2\theta_{13} = 0.071 \pm 0.011$, with a χ^2_{min} per degree of freedom of 6.4/6.

IX. DISCUSSION

The precision to which θ_{13} is determined is crucial to constraining the leptonic CP phase δ [1–4]. The $n\text{H}$ -IBD analysis in this article provides an independent determination of $\sin^2 2\theta_{13}$ and improves the overall precision of θ_{13} .

Given that the uncertainty of the $n\text{H}$ -IBD result is dominated by the systematic uncertainties of the delayed-energy and coincidence-distance criteria, improved precision is foreseen by reducing the uncertainties of the distance criterion with increased statistics, and the delayed-energy criterion with an optimization of the selection. In addition, improved precision will be achieved with a spectral analysis of the prompt-energy spectrum, which is underway. This will also provide a new determination of the mass-squared difference Δm_{32}^2 .

The analysis of $n\text{H}$ -IBDs has helped to maximize the fiducial volume of the ADs to supernova neutrinos [63]. It should also provide an opportunity to reduce the dominant uncertainty of detection efficiency in the measurement of reactor antineutrino flux [44], given the lesser sensitivity of the $n\text{H}$ -IBD analysis to neutron spill-in/out effects. Furthermore, the data-driven techniques developed to study the accidental background and the IBD selection criteria may be useful for other experiments that use or plan to use $n\text{H}$ -IBDs, such as JUNO [27], RENO-50 [28], and LENA [29].

X. CONCLUSION

A sample of about 780000 n H-IBDs was obtained with the 6-AD and full 8-AD configurations of the Daya Bay experiment and was used to compare the number of reactor antineutrinos at far and near halls, yielding a new independent determination of $\sin^2 2\theta_{13} = 0.071 \pm 0.011$. The uncertainty is reduced by 40% compared with the previous n H-IBD result primarily because of the factor of 3.6 increase in statistics, but also because of the 15% and 30% reductions in the uncertainties of the IBD selection efficiency and backgrounds, respectively. The new result is consistent with that from the n Gd-IBD analysis from Daya Bay, providing a valuable confirmation of the n Gd-IBD result. Combining the n H- and n Gd-IBD results provides a new improved determination of $\sin^2 2\theta_{13} = 0.082 \pm 0.004$.

XI. ACKNOWLEDGMENTS

The Daya Bay Experiment is supported in part by the Ministry of Science and Technology of China, the United

States Department of Energy, the Chinese Academy of Sciences, the CAS Center for Excellence in Particle Physics, the National Natural Science Foundation of China, the Guangdong provincial government, the Shenzhen municipal government, the China General Nuclear Power Group, the Key Laboratory of Particle & Radiation Imaging (Tsinghua University), Ministry of Education, the Key Laboratory of Particle Physics and Particle Irradiation (Shandong University), Ministry of Education, the Research Grants Council of the Hong Kong Special Administrative Region of China, the MOST fund support from Taiwan, the U.S. National Science Foundation, the Ministry of Education, Youth and Sports of the Czech Republic, the Joint Institute of Nuclear Research in Dubna, Russia, the NSFC-RFBR joint research program, the National Commission for Scientific and Technological Research of Chile, and the Tsinghua University Initiative Scientific Research Program. We acknowledge Yellow River Engineering Consulting Co., Ltd. and China Railway 15th Bureau Group Co., Ltd. for building the underground laboratory. We are grateful for the ongoing cooperation from the China Guangdong Nuclear Power Group and China Light & Power Company.

-
- [1] K. Abe *et al.* (T2K Collaboration), Phys. Rev. D **91**, no. 7, 072010 (2015) [arXiv:1502.01550 [hep-ex]].
- [2] D. S. Ayres *et al.* (NOvA Collaboration), FERMILAB-DESIGN-2007-01 (2007).
- [3] P. Adamson *et al.* (MINOS Collaboration), Phys. Rev. Lett. **112**, 191801 (2014) [arXiv:1403.0867 [hep-ex]].
- [4] C. Adams *et al.* (LBNE Collaboration), arXiv:1307.7335 [hep-ex] (2013).
- [5] Y. Abe *et al.* (Double Chooz Collaboration), Phys. Rev. Lett. **108**, 131801 (2012) [arXiv:1112.6353 [hep-ex]].
- [6] K. Abe *et al.* (T2K Collaboration), Phys. Rev. Lett. **107**, 041801 (2011) [arXiv:1106.2822 [hep-ex]].
- [7] P. Adamson *et al.* (MINOS Collaboration), Phys. Rev. Lett. **107**, 181802 (2011) [arXiv:1108.0015 [hep-ex]].
- [8] M. Apollonio *et al.* (CHOOZ Collaboration), Eur. Phys. J. C **27**, 331 (2003) [hep-ex/0301017].
- [9] A. Piepke (Palo Verde Collaboration), Prog. Part. Nucl. Phys. **48**, 113 (2002).
- [10] S. Yamamoto *et al.* (K2K Collaboration), Phys. Rev. Lett. **96**, 181801 (2006) [hep-ex/0603004].
- [11] F. P. An *et al.* (Daya Bay Collaboration), Phys. Rev. Lett. **108**, 171803 (2012) [arXiv:1203.1669 [hep-ex]].
- [12] F. P. An *et al.* (Daya Bay Collaboration), Phys. Rev. Lett. **115**, no. 11, 111802 (2015) [arXiv:1505.03456 [hep-ex]].
- [13] J. H. Choi *et al.* (RENO Collaboration), arXiv:1511.05849 [hep-ex].
- [14] T. Abrahao *et al.* (Double Chooz Collaboration), JHEP **1601**, 163 (2016) [arXiv:1510.08937 [hep-ex]].
- [15] F. P. An *et al.* (Daya Bay Collaboration), Phys. Rev. D **90**, no. 7, 071101 (2014) [arXiv:1406.6468 [hep-ex]].
- [16] Y. Abe *et al.* (Double Chooz Collaboration), J. High Energy Phys. **1410**, 086 (2014) [J. High Energy Phys. **1502**, 074 (2015)] [arXiv:1406.7763 [hep-ex]].
- [17] K. Abe *et al.* (T2K Collaboration), Phys. Rev. Lett. **112**, 061802 (2014) [arXiv:1311.4750 [hep-ex]].
- [18] P. Adamson *et al.* (MINOS Collaboration), Phys. Rev. Lett. **110**, no. 17, 171801 (2013) [arXiv:1301.4581 [hep-ex]].
- [19] F. Ardellier *et al.* (Double Chooz Collaboration), hep-ex/0606025 (2006).
- [20] J. K. Ahn *et al.* (RENO Collaboration), arXiv:1003.1391 [hep-ex] (2010).
- [21] X. Guo *et al.* (Daya Bay Collaboration), arXiv:hep-ex/0701029 (2007).
- [22] Y. Abe *et al.* (Double Chooz Collaboration), Phys. Lett. B **723**, 66 (2013) [arXiv:1301.2948 [hep-ex]].
- [23] S. B. Kim (RENO Collaboration) in Neutrino Oscillation Workshop, Otranto, Italy, 7-14 September 2014 (unpublished).
- [24] K. Eguchi *et al.* (KamLAND Collaboration), Phys. Rev. Lett. **90**, 021802 (2003) [hep-ex/0212021].
- [25] T. Araki *et al.* (KamLAND Collaboration), Nature **436**, 499 (2005).
- [26] H. Zhang *et al.* (Super-Kamiokande Collaboration), Astropart. Phys. **60**, 41 (2015) [arXiv:1311.3738 [hep-ex]].
- [27] F. An *et al.* (JUNO Collaboration), arXiv:1507.05613 [physics.ins-det] (2015).
- [28] S. B. Kim, arXiv:1412.2199 [hep-ex] (2014).
- [29] M. Wurm *et al.* (LENA Collaboration), Astropart. Phys. **35**, 685 (2012) [arXiv:1104.5620 [astro-ph.IM]].
- [30] F. P. An *et al.* (Daya Bay Collaboration), Nucl. Instrum. Meth. A **773**, 8 (2015) [arXiv:1407.0275 [physics.ins-det]].
- [31] H. R. Band, R. Brown, J. Cherwinka, J. Cao, Y. Chang, B. Edwards, W. He and K. M. Heeger *et al.*, JINST **7**, P06004 (2012) [arXiv:1202.2000 [physics.ins-det]].

- [32] W. Beriguete, J. Cao, Y. Ding, S. Hans, K. M. Heeger, L. Hu, A. Huang and K. B. Luk *et al.*, Nucl. Instrum. Meth. A **763**, 82 (2014) [arXiv:1402.6694 [physics.ins-det]].
- [33] J. Liu, B. Cai, R. Carr, D. A. Dwyer, W. Q. Gu, G. S. Li, X. Qian and R. D. McKeown *et al.*, Nucl. Instrum. Meth. A **750**, 19 (2014) [arXiv:1305.2248 [physics.ins-det]].
- [34] F. P. An *et al.* (Daya Bay Collaboration), Nucl. Instrum. Meth. A **685**, 78 (2012) [arXiv:1202.6181 [physics.ins-det]].
- [35] F. P. An *et al.* (Daya Bay Collaboration), Nucl. Instrum. Meth. A **811**, 133 (2016) [arXiv:1508.03943 [physics.ins-det]].
- [36] See Supplemental Material at [url] for supplied values.
- [37] P. Vogel and J. F. Beacom, Phys. Rev. D **60**, 053003 (1999) [hep-ph/9903554].
- [38] K. A. Olive *et al.* (Particle Data Group Collaboration), Chin. Phys. C **38**, 090001 (2014).
- [39] X. B. Ma, W. L. Zhong, L. Z. Wang, Y. X. Chen and J. Cao, Phys. Rev. C **88**, no. 1, 014605 (2013) [arXiv:1212.6625 [nucl-ex]].
- [40] T. A. Mueller, D. Lhuillier, M. Fallot, A. Letourneau, S. Cormon, M. Fechner, L. Giot and T. Lasserre *et al.*, Phys. Rev. C **83**, 054615 (2011) [arXiv:1101.2663 [hep-ex]].
- [41] P. Huber, Phys. Rev. C **84**, 024617 (2011) [Phys. Rev. C **85**, 029901 (2012)] [arXiv:1106.0687 [hep-ph]].
- [42] F. P. An, X. C. Tian, L. Zhan and J. Cao, Chin. Phys. C **33**, 711 (2009).
- [43] B. Zhou, X. C. Ruan, Y. B. Nie, Z. Y. Zhou, F. P. An and J. Cao, Chin. Phys. C **36**, 1 (2012).
- [44] F. P. An *et al.* (Daya Bay Collaboration), Phys. Rev. Lett. **116**, 061801 (2016) [arXiv:1508.04233 [hep-ex]].
- [45] F. P. An *et al.* (Daya Bay Collaboration), Chin. Phys. C **37**, 011001 (2013) [arXiv:1210.6327 [hep-ex]].
- [46] T. Skwarnicki, Ph.D. thesis, DESY F31-86-02, Appendix E, 1986; M. J. Oreglia, Ph.D. thesis, SLAC-R-236, Appendix D, 1980; J. E. Gaiser, Ph.D. thesis, SLAC-R-255, Appendix F, 1982.
- [47] J. Yu, Z. Wang and S. Chen, Chin. Phys. C **39**, 056102 (2015) [arXiv:1301.5085 [physics.ins-det]].
- [48] L. J. Wen, J. Cao, K. B. Luk, Y. Q. Ma, Y. F. Wang and C. G. Yang, Nucl. Instrum. Meth. A **564**, 471 (2006) [hep-ex/0604034].
- [49] S. Abe *et al.* (KamLAND Collaboration), Phys. Rev. C **81**, 025807 (2010) [arXiv:0907.0066 [hep-ex]].
- [50] F. P. An *et al.* (Daya Bay Collaboration), Phys. Rev. Lett. **112**, 061801 (2014) [arXiv:1310.6732 [hep-ex]].
- [51] F. F. Khalchukov, E. V. Korolkova, V. A. Kudryavtsev, A. S. Malguin, V. G. Rysanii, O. G. Ryazhskaya, G. T. Zatsepin and O. Saavedra, Nuovo Cim. C **18**, 517 (1995).
- [52] T. Hagner, R. von Hentig, B. Heisinger, L. Oberauer, S. Schonert, F. von Feilitzsch and E. Nolte, Astropart. Phys. **14**, 33 (2000).
- [53] Q. j. Li, Z. Wang, J. f. Lv, X. b. Yan, W. q. Jiang and J. f. Chang, doi:10.1109/NSSMIC.2009.5402197
- [54] Y. F. Wang, V. Balic, G. Gratta, A. Fasso, S. Roesler and A. Ferrari, Phys. Rev. D **64**, 013012 (2001) [hep-ex/0101049].
- [55] J. Liu *et al.*, Nucl. Instrum. Meth. A **797**, 260 (2015) [arXiv:1504.07911 [physics.ins-det]].
- [56] W. Q. Gu, G. F. Cao, X. H. Chen, X. P. Ji, G. S. Li, J. J. Ling, J. Liu, X. Qian, and W. Wang, arXiv:1512.00295 [physics.ins-det].
- [57] S. Agostinelli *et al.*, Nucl. Instr. Meth. A **506**, 250 (2003); J. Allison *et al.*, IEEE Trans. Nucl. Sci. 53 No. 1, 270 (2006).
- [58] M. B. Chadwick, M. Herman, P. Oblozinsky *et al.*, Nuclear Data Sheets **112**, 2887 (2011).
- [59] H. R. Band, J. J. Cherwinka, E. Draeger, K. M. Heeger, P. Hinrichs, C. A. Lewis, H. Mattison and M. C. McFarlane *et al.*, JINST **8**, P09015 (2013) [arXiv:1307.1089 [physics.ins-det]].
- [60] W. Q. Jiang, S. D. Gu, J. Joseph, D. W. Liu, K. B. Luk, H. Steiner, Z. Wang and Q. Wu, Chin. Phys. C **36**, 235 (2012).
- [61] H. R. Band, J. J. Cherwinka, L. S. Greenler, K. M. Heeger, P. Hinrichs, L. Kang, C. A. Lewis and S. F. Li *et al.*, JINST **8**, T04001 (2013) [arXiv:1206.7082 [physics.ins-det]].
- [62] M. He, arXiv:1501.06969 [physics.ins-det] (2015).
- [63] H. Wei, L. Lebanowski, F. Li, Z. Wang and S. Chen, Astropart. Phys. **75**, 38 (2016) [arXiv:1505.02501 [astro-ph.IM]].